Julius-Maximilians-Universität Würzburg
Fakultät für Physik und Astronomie
Lehrstuhl für Astronomie

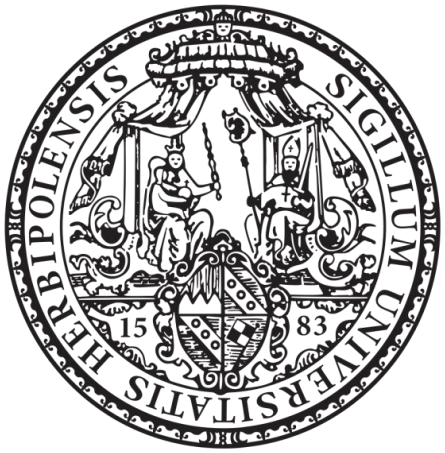

Bachelor Thesis

X-ray Analysis of the AGN NGC 1052 with XMM-Newton

Author: Constanze Seibert
Supervisor: Prof. Dr. Matthias Kadler
Date of Submission: March 29, 2019

1 Abstract

In this work, Active galactic nulcei (AGN) and their X-ray emission are studied.
AGN are sources with a relative high luminosity which are emitting radiation over the entire electromagnetic spectrum. Although these sources show very different characteristics, they can be explained in an unification model. Their spectrum in the X-ray range can be described in four basic model components, which are primarily generated by bremsstrahlung and inverse Compton scattering.
The prototypical LINGER galaxy, NGC 1052, will be analyzed with already existing X-ray data of the *XMM-Newton* satellite. The extraction of the data, basing on the observation from 7th January 2017 is carried out with the Science Analysis System (SAS), whereby a source and background region of 35 to 40 arcseconds is selected on all three detectors of the EPIC camera. The resulting light curves are examined on variability. Since no variability was found, the spectra of NGC 1052 are analyzed.
The spectra analysis was done with the Interactive Spectral Interpretation System (ISIS), while the spectrum of pn was used primarily because of the larger effective area. Basing on already excisting studies of NGC 1052, a partial covering model is used to fit a soft X-ray component described with a thermal plasma and a highly absorbed powerlaw. Additionally, there are discussions about the existence of an relativistically broadened $Fe\ K\alpha$ emission line. Therefore, a relativistic Compton reflection model is used. Within this model fit, no evidence for a such a broad feature is found, even without the additional spectra of the MOS detectors.

2 Zusammenfassung

Diese Arbeit basiert auf der Untersuchung von Aktiven Galaxiekernen und speziell ihre Röntgenemission.
Aktive Galaxiekerne sind sehr helle Quellen, die über das gesamte elektromagnetische Spektrum Strahlung emittieren. Sie weisen unterschiedliche Charakteristika auf, lassen sich aber durch ein einheitliches Schema erklären. Ihr Spektrum im Röntgenbereich kann durch vier grundlegende Modellkomponenten beschrieben werden, die hauptsächlich durch Bremsstahlung und inverser Comptonstreuung entstehen.
Die prototypische LINER Galaxie NGC 1052 wird anhand vorliegender Röntgendaten des *XMM-Newton* Satelliten im Detail analysiert. Diese Daten vom 17. Januar 2017 werden mit dem Science Analysis System (SAS) extrahiert, wobei eine Quellregion, sowie eine Hintergrundregion gleicher Größe von 35-40 Bogensekunden auf allen drei Detektoren der EPIC Kamera ausgewählt wird. Die resultierenden Lichtkurven werden auf Variabilität untersucht. Nachdem keine Variabilität in den Lichtkurven zu sehen war, wurden die Spektren dieser Detektoren analysiert.
Die Spektralanalyse erfolgte mittels dem Interactive Spectral Interpretation System (ISIS). Hauptsächlich wurde das Spektrum von pn genutzt, da dieser Detektor eine größere effektive Fläche hat. Basierend auf vorherigen Röntgenstudien dieser Quelle, wurde ein "Partial Covering"-Szenario angesetzt, welches gut an die Daten gefittet werden konnte. Zusätzlich gibt es bei NGC 1052 Diskussionen über eine vorhandene Verbreiterung der Eisen Emissionslinie, welche durch relativistische Effekte resultiert. Deshalb wurde ein relativistisches Compton-Reflexionsmodell an das Spektrum gefittet. Das Modell konnte mit einem ausreichenden Signal-zu-Rausch-Verhältnis an die Daten gefittet werden. Es konnte jedoch keine relativistisch verbreiterte Eisenlinie nachgewiesen werden. Auch die zusätzlichen Spektren von den MOS Detektoren führten zu keinem Nachweis.

Contents

3 Theory of AGN

The spectra of normal galaxies in the optical and near-infrared are dominated by the emission of stars, gas and dust. Active galaxies have a much broader spectral energy distribution and often show emission in the full range of the electromagnetic spectrum from the radio to the X-ray regime. Their emission originates mainly from a small central region, called the active galactic nucleus (AGN). In many cases the luminosity of an AGN exceeds the light of its host galaxy by far. The energy source of this emission originates in the accretion of matter onto a supermassive black hole (SMBH) (Hoyle & Fowler, 1963). The small emission region of the AGN consists of multiple components showing different physical processes, which will be briefly discussed in the following sections. If not highlighted otherwise, this chapter is based on the textbook "Extragalactic Astronomy and Cosmology" by Schneider (2015).

3.1 Classifications

AGN form a family of different types, which differ in their spectral properties, their total luminosities and the ratio of the luminosity of the nucleus to the stellar light of the host galaxy. A major distinguish factor is the so-calles radio loudness of AGN. As radio-quiet AGN are typically missing visible jet structures, which would emit strongly in the radio wavebands, their ratio of radio to optical emission is low (Kellermann et al., 1989). Further classifications are:

Seyfert galaxies

Seyfert galaxies (Seyfert, 1943) are usually spiral galaxies and are divided into subclasses, based on the visible optical spectral lines. Type 1 shows continuous emission with broad and narrow lines on top, while type 2 shows weak continuum emission and only strong narrow lines. Typically, Seyferts they are radio-quiet.

LINER

Low-Ionization Nuclear Emission Line Region galaxies (LINERs) are very similar to Seyfert Type 2 with a difference in the emission of the optical spectra. LINERs' continuum emission is weaker, but the low-ionization emission lines are stronger.

Quasars

Quasi Stellar Radio sources (Quasars) were defined as star-like looking objects, based on quasi stellar objects (QSO). QSO are similar to Seyferts, but their nuclei are much brighter. Quasars are usually radio-quiet with a higher redshift. A flat spectrum in the radio band results in an underclass of Flat Spectrum Radio Quasars (FSRQ).

Radio Galaxies

Radio galaxies can be subdivided into broad-line radio galaxies (BLRG) and narrow-line radio galaxies (NLRG) and are usually embedded in elliptical galaxies. Besides the classification with respect to the spectra, radio galaxies can be distinguished according to their jet morphology. According to Fanaroff & Riley (1974), this is done with two classes of so-called Fanaroff-Riley galaxies (FR1 & FR2). FR1 are core-dominated AGN with symmetrical jets ending in plumes. FR2 are jet-lobe-dominated with often only one weak jet ending in radio lobes (Krolik, 1999).

Blazars

Blazars are characterized by high variability on short time scales and mainly on a strong continuous spectrum with weak or no emission lines. Galaxies classified as blazars are either BL Lacertae (BL Lac) object or flat spectrum radio quasars (FSRQ) based on their total luminosity. Blazars are radio-loud and due to the viewing angle is directly into the jet, they are the most luminous AGN.

3.2 Unification model

Based on the AGN unification scheme by Urry & Padovani (1995), a large fraction of AGN classes can be explained by viewing the same object, an accreting black hole surrounded by dust, from different angles. Figure 3.1 illustrates the basic structure of an AGN and shows the difference classifications depending on the viewing angle.
The SMBH in the center of an AGN accretes material from the gas and dust torus that orbiting the black hole. Due to the conservation of momentum the material forms an accretion disk whose axis is approximately identical to the rotational axis of the torus and jet axis in radio-loud AGN. Because of differential rotation and particle collision in the disk potential energy is radiated away. The loss of energy consequently decreases the orbot of the disk material, which falls onto the black hole. Charged particles in the accretion disk can be forced away from the disk due to magnetic fields of the disk itself. The resulting outflows of charged particles perpendicular to the disk create the observed jets.
The closer the material is orbiting the black hole, the faster it becomes, and due to the large velocity dispersion within the accretion disc, the emission lines in spectra are broad. This region is therefore called broad line region (BLR). Material far away from the central engine has a smaller velocity dispersion and shows only narrow emission lines, therefore marking the narrow line region (NLR). The inclination of the system is measured with respect to the accretion disk. If we observe an AGN from the top with an unblocked view to the accretion disc, we would see this source from an inclination angle of 0°. In case of a radio-loud AGN, we would classify this source as a blazar, because we would look directly into the jet. In a radio-load AGN this would be a look into the jet and the classification is a blazar. In a radio quiet AGN this viewing angle would represent a Seyfert Type 1 galaxy, because we can see both the NLR and the BLR. For an increased inclination angle, a dusty absorber, also called torus, can block the view into the BLR for the observer. In this case the AGN is classified as Seyfert Type 2 for a radio-quiet galaxy or as NLRG for a radio-loud AGN, respectively.

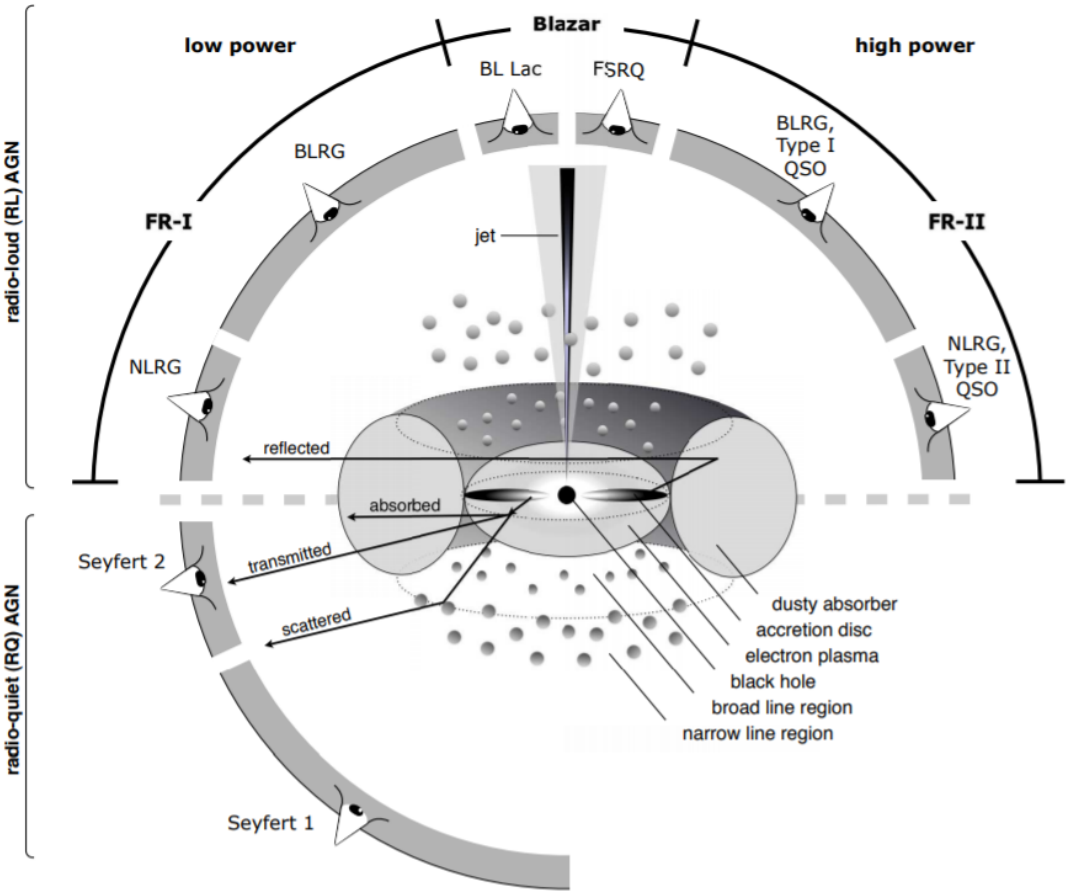

Figure 3.1: Unification model of AGN with respect to the different viewing angles on the AGN. The upper part represents a radio-loud AGN. With an edge-on view through the dusty absorber (torus), only the NLR is visible. Perpendicular to the accretion disk, one looks directly into the jet. For radio-quiet AGN no jets are present. *Credit: Beckmann & Shrader (2012)*

3.3 X-ray emission in AGN

The most energetic X-ray radiation is expected to originate close to the SMBH. Therefore, X-ray emission reveals the processes of the innermost region of AGN. This work is based on the assumptions by Fabian (2006), who describes an X-ray spectrum using four model components. The spectra are characterized by a hard powerlaw which may turnover at a few hundred keV, a soft excess, a reflection component and the iron emission line as visualized in Fig. 3.2. The powerlaw $S_\nu \propto \nu^{-\alpha}$ is characterized by its slope, which is steeper for radio-quiet AGN and flatter for radio-loud AGN (Schneider, 2015). In the lower energy range the spectrum seems steeper than the powerlaw, which is called the 'soft excess'. Beyond energies higher than ~ 100 keV the spectrum experiences a cut-off. This is called the high energy cut-off.
The decomposition of the spectrum into these four components (powerlaw, soft excess, iron

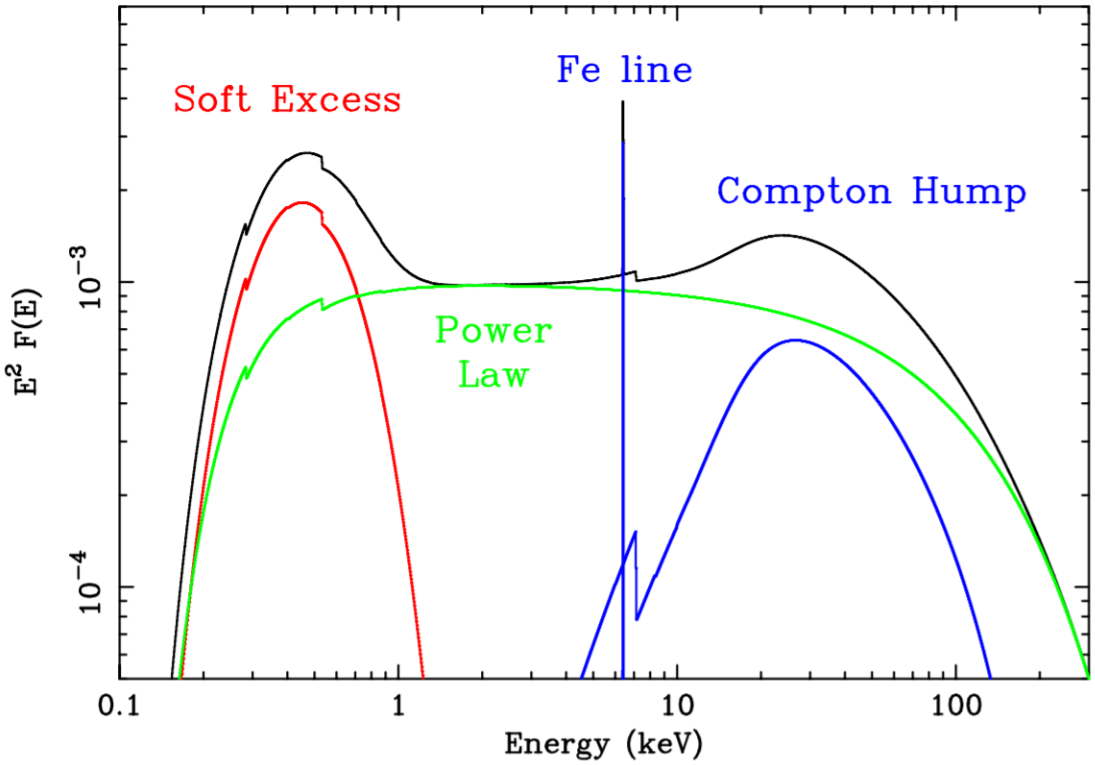

Figure 3.2: Sketch of a typical X-ray spectrum of an AGN with four components of a standard model. *Credit: Fabian (2006)*

line and compton hump) is based on the idea of how X-ray emission is generated in AGN. The following are major contributing effects to the production of X-rays will be discussed.

Bremsstrahlung Bremsstrahlung is electromagnetic radiation that is produced when a charged particle, for example an electron, is accelerated. Every change in speed of a charged particle generates radiation. Generally, electron-proton collisions dominate, because the electron-proton system possess a significant electric dipole. When the electron velocities become relativistic, the radiation in other moments become comparable to the electric dipole radiation in strength. The contributions of several other kinds of collision need to be taken into account, when $k_B T \sim m_e c^2$ (Krolik, 1999).

Inverse Compton scattering If a photon scatters a electron at rest, the photon can transfers part of its energy to the electron, which then recoils. This effect is called the Compton effect. In the event that the electron is not stationary and has a much higher energy than the photon, this effect can reverse. In that case, the electron transferes energy to the photon, which is called the inverse Compton effect. Regions of hot electron gas surrounding the accretion disk produce inverse Compton-scattered radiation from optical light emitting from the disk.

3.4 NGC 1052

In my thesis, data from the AGN NGC 1052 is analyzed. Therefore, I would like to present an overview of previous studies of that source.
NGC 1052 is a giant elliptical galaxy with strong optical emission lines, classfied as a prototypical LINER galaxy, and contains a luminous H_2O maser (Weaver et al., 1999), which has only been confirmed for one other elliptical galaxy. The source has the following coordinates in J2000: RA=$02^h41^m04^s7985$ Dec=$-08°15'20''.751$. The distance to the galaxy is approx. 19.6 Mpc according to the NASA/IPAC Extragalactic Database (NED)[1]. In this work, a redshift of $z = 0.005$, based on Knapp et al. (1978), was used for the analysis. In several radio observations this AGN shows a twin-jet system with south-west orientation, which can be used to estimate the inclination angle to $\sim 86°$ (Baczko et al., 2016). Very long Baseline Interferometry (VLBI) observations revealed that the jets are extending from a single core without any indication of absorption due to the obscuring torus. Earlier analyzed X-ray observations of this source indicate an extended X-ray emission in addition to the nucleus emission (Kadler et al., 2002). The first detailed studies of the spectrum of NGC 1052 were made with *ASCA* (Weaver et al., 1999) and *BeppoSAX* (Guainazzi et al., 2000) observations. Guainazzi (2000) found a hard and strongly absorbed continuum, and Brenneman et al. (2009) and Brenneman, analysing *Suzaku* observations, considered a relativically broadened iron line a few gravitational radii away from the central region. A relativistic broadened iron line could yield information of the accretion disk, as well as information about possible disk-jet interaction. Since those broad lines are typically not detected in radio-loud AGN, it would be very interesting to find one in this source. Kadler et al. (2004) implementing the first *XMM-Newton* observation of this source, modeled a spectrum with a reflection model, containing a relativistically broadened iron line. Kadler (2004) suggested also the possibility to measure the black hole spin, if the interpretation of the broad feature as a relativistic line is true.

[1] NED (https://ned.ipac.caltech.edu, March 24, 2019)

4 X-ray astronomy

4.1 Evolution of X-ray astronomy

The earth's atmosphere is impermeable for X-rays, which is why extraterrestrial X-ray emission stayed hidden from us until the 1950s. After World War II, military rockets and balloons equipped with radiation detectors only left the atmosphere for a few minutes. The first astronomic X-ray source detected was our sun's corona in 1949. *Uhuru*, launched in 1970, was the first satellite entirely dedicated to X-ray astronomy. This satellite extended the on-board observation time from minutes to years (Santangelo & Madonia, 2014). In three months the entire sky could be studied systematically and many new sources could be localized with a precision of about 1 arc minute (Giacconi, 2003). The next huge step in the history of X-ray astronomy was taken by the *Einstein* Observatory in 1979, equipped with the first Wolter telescope on board, which provided sensitivity to observe several galactic X-ray sources like stars, binary sources, supernovae remnants, and additionally extragalactic sources like galaxies, cluster of galaxies and active galactic nuclei (AGN) (Arnaud et al., 2011). In 1990, *ROSAT*, a German X-ray satellite, was launched. This mission resulted in the first image of the complete X-ray sky and led to the discovery of around 80,000 X-ray sources. A *ROSAT* catalogue has been compiled, which contains positions and counting rates of more than 100,000 X-ray sources. This catalogue of X-ray sources and their properties still form the basis for numerous in-depth observations with later X-ray missions such as the ESA *XMM-Newton* mission and the NASA *Chandra* mission (both operational in Earth orbit since 1999) [1]. Among the most important discoveries are the realisation that the cosmic X-ray background radiation is caused by unresolved quasars and active galaxies (Mushotzky et al., 2000).
The formation of X-rays in astronomical objects is always associated with very hot plasma ($\approx 10^6$ K) or non-thermal processes (Schneider, 2015). Therefore, *XMM-Newton*'s observational objects include star formation regions, supernova remnants, variable stars, galaxy clusters and AGN. The study of the outer atmospheres of stars can contribute to the understanding of the heating of the coronary gas and the history of the formation of a star. Several X-ray sources change their brightness over time on very different time scales. *XMM-Newton* is able to detect variability in detail and is used, for example, to study different types of AGN, their structures and physical processes.
Nowadays, almost every X-ray telescope in space is equipped with a Wolter telescope on board. In Fig. 4.1, the telescope structure of a Wolter telescope is shown. The mirror arrangement is made up of multiple nested metallic paraboloid mirrors, each of which is followed by a hyperboloid. Often the mirrors consist only of thin foils coated with metal. In order to focus X-rays one makes use of total reflection of heavy elements with refraction index $n < 1$. Therefor total reflection occurs at the grazing incidence on the surfaces. This design is needed

[1] (https://www.dlr.de/dlr/desktopdefault.aspx/tabid-10424/, Jan 15, 2019)

because the surfaces of optical telescopes would either transmit or absorb the high-energetic particles (Bergmann et al., 2002).

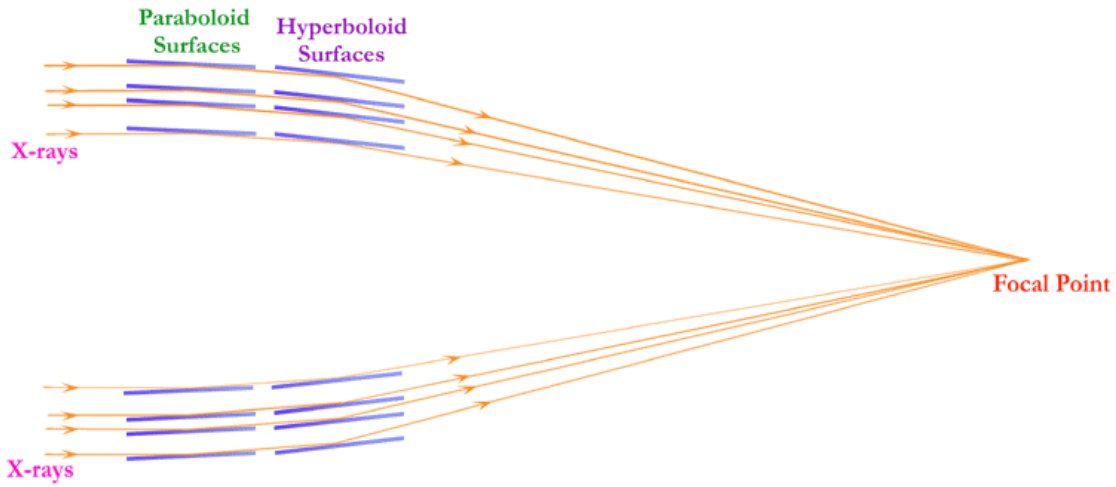

Figure 4.1: Schematic representation of a Wolter telescope
The mirrors consist of paraboloids ending in hyperboloids. The light reflects on the smooth surface and does not penetrate through the surface. *Credit: NASA/Chandra*

4.2 XMM-Newton Observatory

The *X-ray Multi-Mirror (XMM) Newton* Observatory from the European Space Agency (ESA) was launched in December 1999. In Fig. 4.2 the structure of the different modules on the spacecraft is illustrated. The *XMM-Newton* Observatory is equipped with two different types of telescopes. One is the Optical Monitor (OM) - a 30 cm long optical/UV telescope. In addition, there are three Wolter-I telescopes, which detect X-ray photons. The combination of both types of telescopes in one spacecraft offers the possibility to observe the optical/UV and the X-ray band simultaneously. Each Wolter-I telescope consists of 58 cylindrically nested mirrors, made of nickel and coated with a thin layer of gold, and having a focal length of 7.5 m.

4.2.1 The EPIC camera and the RGS

X-ray photons are reflected on the mirror surfaces and are focused into the European Photo Imaging Camera (EPIC), which combines three Charge Couple Device (CCD) cameras. Two of these cameras are Metal Oxide Semi-conductors (MOS). They are installed behind the focussing optics, which are equipped with the gratings of the reflection grating spectrometer (RGS). The gratings redirect about half of the incoming rays to the RGS detector, so that about 44% of the original incident flux reaches the MOS cameras[2], see Fig. 4.3 below. The reflecting grating spectrometer fans out the different wavelengths, such that spectral lines in

[2](https://www.cosmos.esa.int/web/xmm-newton/technical-details-epic, Jan 15, 2019)

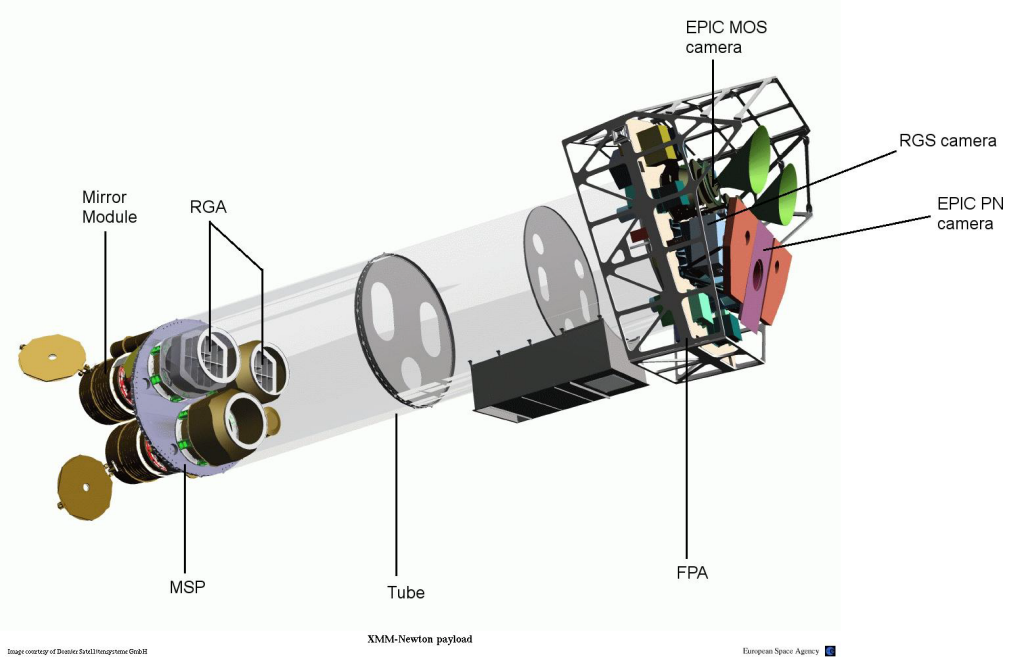

Figure 4.2: Illustration of the XMM-Newton payload
On the top right is the Focal Point Assembly (FPA) with the detectors EPIC MOS (green/black) and pn (violet) as well as the Reflecting Grating Spectrometer (RGS, light blue). On the left, the optical monitor (OM) is covered by the Mirror Support Platform (MSP) and the mirror modules and Reflecting Grating Arrays (RGA) are visible. *Credit: Image courtesy of Dornier Satellitensysteme GmbH, modified by Annika Kreikenbohm.*

the energy range 0.1-2.5 keV, where most lines are occuring, can be resolved. The spectral resolution $\frac{E}{dE}$ lies between 200 and 800 in the energy range of 0.35 up to 2.5 keV (ESA, 2012). The third X-ray telescope uses pn-type CCDs in the focal plane, where the photon beam is directed onto the camera without interruptions.
The EPIC cameras offer the possibility of extremely sensitive images over an entire field of view (FOV) of the telescope of 30 arc minutes and in the energy range from 0.2 to 12 keV (Lumb et al., 2002), whereby effectively only the range up to 10 keV can be used. They provide an energy resolution $\frac{E}{dE}$ of 20-50 that depends on the photon energy and event pattern due to statistical variations within the CCD as well as electronic noise and readout noise (more details in section 4.2.2). Despite the energy resolution, the two types of detectors differ in some essential aspects (see comparison in Table 4.1). Figure 4.4 shows a sketch of the FOV of the EPIC MOS in comparison to the EPIC pn camera. In the focal plane of every MOS camera there are seven front illuminated CCDs each with a size of 10.9 x 10.9 arcminutes. The central CCD is located at the focal point on the optical axis of the telescope, while the outer six are indented by 4.5 mm to follow the curvature of the focal plane and improve the focus for sources on the outer pixels. In comparison, the pn camera achieves uniform detector quality over the entire FOV by the monolithic production of twelve backside illuminated CCDs, each with a size of 13.8 x 4.4 arcminutes (3 x 1 cm). The four individual quadrants are operated in

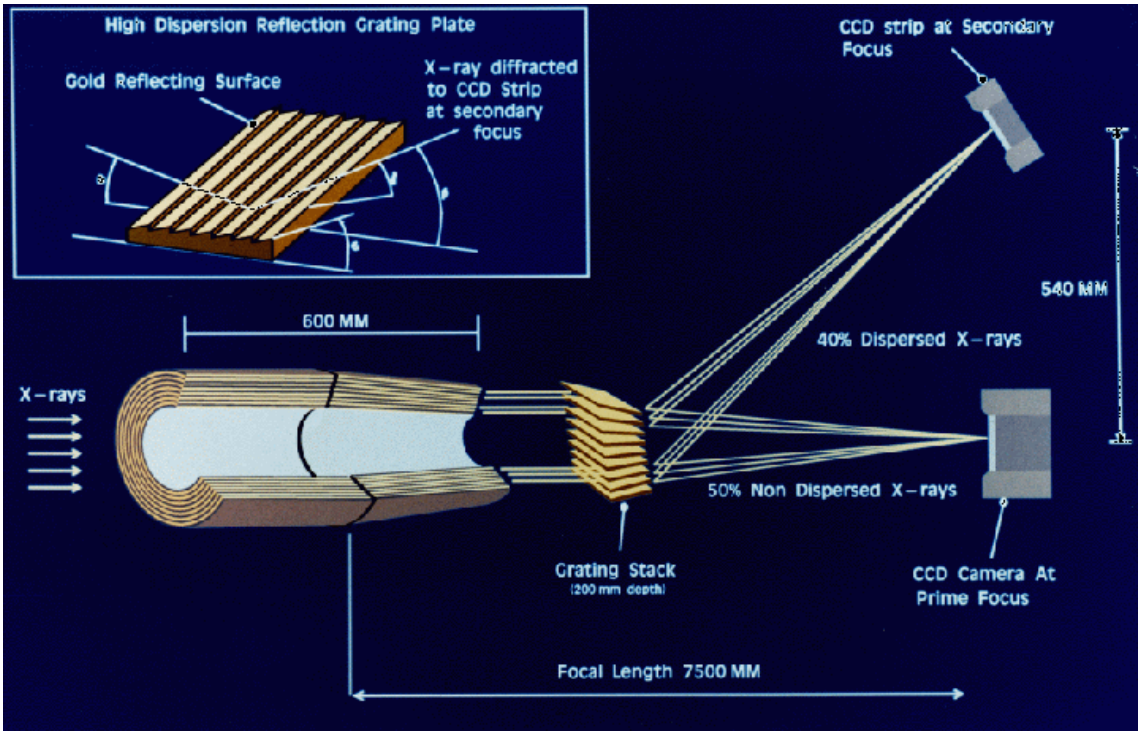

Figure 4.3: Geometry of the RGS
The gratings of the Reflection Grating Assembly are located between the mirrors and the EPIC MOS cameras. They deflect about 40% of the light to the RGS focus cameras and transmit about 42% of the light to the EPIC, while the rest of the light is absorbed by the structures. *Credit: ESA/XMM-Newton (https://heasarc.gsfc.nasa.gov/docs/xmm/about_mirrors.html, Jan 18, 2019)*

parallel, each with three pn-CCD subunits in 200 x 64 pixel format (ESA, 2012). In addition to the geometric arrangement of the CCD arrays, the device design is also very different. When determining the effective area of all cameras, their quantum efficiency must be taken into account. The current quantum efficiency curve is illustrated in Fig. 4.5 for both CCD types. The quantum efficiency of the EPIC MOS chips limits the energy band pass at its high energy end, while the pn camera can detect photons with a high efficiency of up to 15 keV. The quantum efficiency of MOS-CCDs is a smooth function except near the edges of silicon and oxygen. The drop in quantum efficiency function of the pn CCD at the lowest energies is also caused by the properties of the silicon edge (ESA, 2012). The dependency of the quantum efficiency has to be kept in mind for section 5.

4.2.2 EPIC Background

Charged coupled devices (CCDs) are light-sensitive electronic components that are used to "count photons". The technology of CCDs is based on the internal photoelectric effect (Howell, 2006). Incident light transfers its energy to electrons of the semiconductor material (e.g.

Instrument	EPIC MOS	EPIC pn	RGS	OM
Bandpass	0.15-12 keV	0.15-15 keV	0.35-2.5 keV	180-600 nm
Oribital target visibility	5-135 ks	5-135 ks	5-135 ks	5-145 ks
Sensitivity	$\sim 10^{-14}\ \frac{\text{erg}}{\text{scm}^2}$	$\sim 10^{-14}\ \frac{\text{erg}}{\text{scm}^2}$	$\sim 8 \cdot 10^{-5}$	20.7 mag
Field of View (FOV)	$30'$	$30'$	$\sim 5'$	$17'$
PSF (FWHM/HEW)[a]	$5''/14''$	$6''/15''$	-	$1.4'' - 2.0''$
Pixel size	40 μm ($1.1''$)	150 μm ($4.1''$)	81 μm ($9 \cdot 10^{-3}$ Å)	$\sim 0.48''$
Timing resolution	1.75 ms	0.03 ms	0.6 s	0.5 s
Spectral resolution	~ 70 eV	~ 80 eV	0.04/0.025 Å	350

Table 4.1: Important physical characteristics of XMM-Newton's instruments.

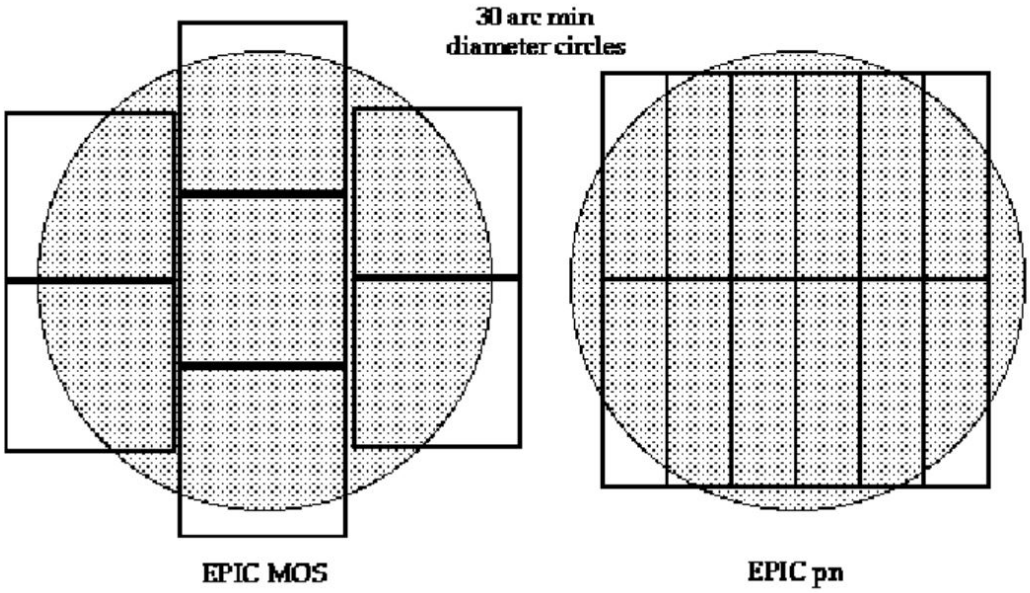

Figure 4.4: Sketch of the field of view of the EPIC camera MOS (left) and pn (right) with a shaded circle of 30' diameter. *Credit: XMM-Tools (ESA, 2012)*

silicon), which the CCD is made of. Hence, a number of negatively charged free electrons and positively charged "holes" are created proportionally to the energy of the photon. The effectiveness of this process is described with the quantum efficiency

$$\text{QE} = T \cdot A, \tag{4.2.1}$$

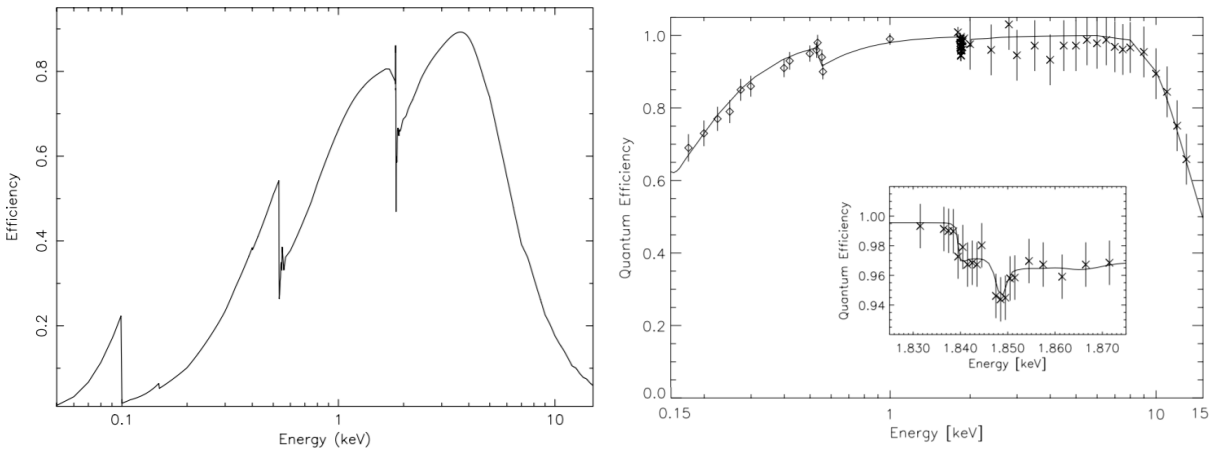

(a) Quantum effiency of the MOS detector.

(b) Quantum effiency of the pn detector.

Figure 4.5: Quantum efficiency of the EPIC cameras, MOS (left panel, (Turner et al., 2001)) and PN (right panel, (Strüder et al., 2001)) as a function of photon energy.

depending on the probability T for the transmission of photons and the probability A for the absorption of photons in silicon at a given wavelength. While QE=100% describes an ideal detector, where every photon generates an output. In order to keep track of the origin of the photons, many separated, micrometer-scaled semiconductor crystals are aligned in a grid. The larger the area of the pixels, the higher the light sensitivity of the CCD sensor, but the smaller the image resolution for the same sensor size. Since the free electrons would recombine with the crystal structure within 100 μs, they are collected in a potential pot. These are also called gates and there are typically three of them per pixel (Howell, 2006).
There are different components that affect the background of the EPIC camera. First there is the instrumental background, which shows no variation during an observation. At energies below 200 eV readout noise coming from the detector becomes important. There is also a noise component resulting from the interaction of the particles in the detector structures, which can be characterized by a flat spectrum predominant at energies above a few keV (ESA, 2012). Other common pixel errors that can falsify an image are e.g. hot or cold pixels. Cold pixel appear as a permanently black pixel in the image as it is damaged and cannot absorb light. Furthermore, hot pixels are constantly overexposed. They have a much higher dark charge rate than their neighbors and are therefore called "hot pixels". Time-varying voltages at the pixels allow the extracted electron-hole pairs to be moved in the direction of the read-out anode. So one defective pixel affects the whole row (Bergmann et al., 2002).
In addition, there is a particle-induced background that cannot be suppressed. This background can be divided into soft protons and cosmic rays. External flares are characterized by rapid variability and can be attributed to soft protons with energies smaller than a few 100 keV. These soft protons affect 30% to 40% of *XMM-Newton* observation time. They originate from solar soft protons, which are accelerated by the magnetosphere, get trapped in the earth's atmosphere and directed by the X-ray mirrors onto the detectors (Carter & Read, 2007). The cosmic particle component is a more stable internal one, which results from the interaction

of high-energy particles (with energies greater than several 100 MeV) with the surrounding structure of the detectors and possibly the detectors themselves (ESA, 2012).
Most importantly, there is a cosmic X-ray background (CXB), which are X-ray photons from unresolved sources hitting the detector (ESA, 2012). This photon noise can be devided into a hard and a soft component. The hard X-ray background mainly originates from unresolved AGN within the FOV and shows no variation during observations (Carter & Read, 2007). This component dominates below 5 keV, while the soft X-ray photon background is more present at energies below 1 keV. The soft X-ray background originates from single reflections outside the FOV, like the Galactic Disk and Galactic Halo, as well as from the Solar Wind Charge Exchange (Carter & Read, 2007).
The EPIC background components are extremely complicated. To analyse specific sources, the knowledge of the components of the background are required.

5 Data Extraction and Analysis

The data extraction was performed with the Science Analysis System (SAS) version 16.0.0, which was specially developed by the *XMM-Newton* Science Operation Center (SOC) for the reduction and analysis of *XMM-Newton* data. NGC 1052 was observed on January 17, 2017 under the Observation ID 0790980101 for a total observation time of 70.5 ksec ($\approx$ 19.58 h). The observation time can vary for each instrument. In the following, the extraction of data from the EPIC cameras will be examined. All cameras operated in full frame mode. To block optical starlight a thin filter (PN) and medium (MOS) filter were used[1]. All EPIC CCDs work in photon counting mode with a fixed image readout frequency. They generate event lists, i.e. tables with one input line per received event, which, among other things, list attributes of the events such as the position at which they were registered, their arrival time and their energies (ESA, 2012). The extraction for OM and RGS is not part of this work and is therefore not explained. The following information on extraction of *XMM-Newton* data is based on the XMM manual (ESA, 2012).
Originating from the Observation Data Files (ODF) and the Catalogue of Calibration Files (CCF) the extraction process starts. The ODF contains FITS-files for every camera and CCD sensors with general information about the observation, such as the exposure time, the used instruments and filters as well as the exposure modes. The CCF is needed to identify the given time of the observation. A calibration index file (cif) is generated via the command *cifbuild* in order to identify necessary calibration files. The calibration files are provided by the *XMM-Newton* Science team and have to be updated to the system with *odfingest*, which results in the creation of a new file. Then the ODF will be reprocessed to get calibrated and concatenated EPIC event lists.

5.1 Generating event lists

In the next step of extraction, the latest software developments and updated calibration files are taken into account. *epproc* creates updated event lists and a list of bad pixel positions for each CCD of the EPIC/pn instrument, with *emproc* for the EPIC/MOS respectively. Pixels classified as bad will not be considered for further data analysis. Usually a GTI file will be created when filtering for flaring particle background, but using the qualifier *withgtiset=yes gtiset=mygtifile.fits filterevents=yes* it is possible to load an extern Good Time Interval (GTI) file, named here "mygtifile.fits". The event lists are the starting point of the analysis and interpretation of *XMM-Newton* data.

[1] *XMM-Newton* Observation Log(http://xmm2.esac.esa.int/external/xmm_obs_info/obs_view_frame.shtml, March 11, 2019)

5.2 Filtering for flaring particle background

The detectors of the *XMM-Newton* telescope are not able to automatically differ between the photons from the observed source and other high energy particles hitting the detector (e.g. protons). False detection of photons usually appear as single pattern events with energies higher than 10 keV. Light curves are created for PN and MOS by selecting events with energies above 10 keV from the whole detector. Different qualifiers were set for pn and MOS detectors. For all detectors only those events were selected in which a photon was detected by a single pixel.

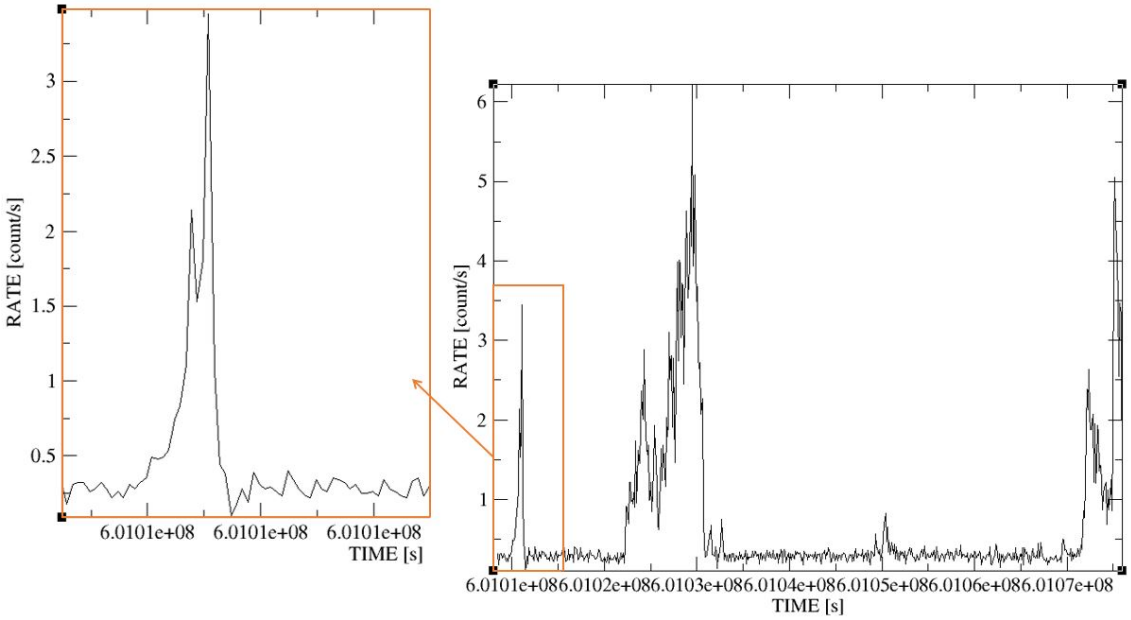

Figure 5.1: Examplary lightcurve of the full FOV of the pn detector. The count rate is plotted versus the *XMM-Newton* mission time. The orange rectangle shows a zoom into a flaring component of the lightcurve.

Checking the produced lightcurve in Fig. 5.1, which has been extracted for the complete detector, for flaring behaviour, one can determine a threshold for rejecting background flares. The rate is plotted against the time, where the rate represents the counts of photons per second that hit the detector area. The time is given in the *XMM-Newton* mission time in seconds, which started on January 1st, 1998. Figure 5.1 is only used to visualize the process of setting a threshold for the rate for the background. One can see a very variable lightcurve for the full detector, identifying high background flaring during the observation time. Usually the threshold for excluding flares is set to a count rate of $<= 0.4$ for pn and $<= 0.35$ for the MOS respectively, which would be also sufficient for this observation. To filter an EPIC event list for flaring particle background, *tabgtigen* is used to generate a GTI file, which defines the usable time intervals. Light curves for NGC 1052 are created for the recommended count rate limits. However, a detailed study described in section 5.3 shows that this limit is not able to fully filter out the flaring periods. After carefully investigating the background level of the source,

a GTI file was generated using *counts* <= 100, to filter all counts above 100. The GTI file is then used to filter the event list again with a set of a minimal energy of 1.5 eV ($PI > 150$) for pn and MOS. The filtered event lists are used for further analysis.

5.3 Selection of source region

The X-ray spectrum of an individual source, e.g. NGC 1052 in this thesis, requires the selection of the source region as well as a background region on the detectors image. The pn image of the analysed ovservation of NGC 1052 is shown in Fig. 5.2 in a logarithmic heat color scale. The 12 CCD sensors of the detector are visible.
Figure 5.3 shows a zoom into the source region of NGC 1052, with the source and background regions in green. Since the source lies at the edge of the CCD, it was not possible to define a circular region of 40 arcsec as recommended, so a region of 35 arcsec was chosen for both the source and the background. The best conditions for the extraction of the source are given for a background region on the same CCD and for similar y-distance as the source region. It was not possible to lay the background on the same y-distance, because the source lay on the edge of the CCD. For extended sources such as NGC 1052, background extraction should be far away from the selected source region (Carter & Read, 2007). Also note that there are no other sources in the background region. The color scale on the x-axis shows the photon counts, where black means no photons hit the pixel of the detector, red means several photons are detected and white means a huge photon abundance.
NGC 1052 is not a typical point source. Some counts belonging to the source are outside the green region. But since the largest number of photons lies within this range and this work is about the X-ray emission of the nucleus, it should not be significantly different. To prove this assumption, different regions were extracted and the lightcurves are compared in section 5.3.
Figure 5.4 shows the detectors image of MOS1. Three out of seven CCDs were excluded from further analysis during the extraction process. NGC 1052 is clearly visible in the central CCD. Zooming into the central CCD, Fig. 5.5 shows the source and the background regions, both with a diameter of 40 arcseconds. The background region is placed in the same y-distance as the source region.
An image of the MOS2 detector is shown in Fig. 5.6. NGC 1052 lies in the middle of the central CCD. One can see the dead column crossing the source region caused by a defective pixel (see section 4.2.2 for more information about pixel defects). This pixel defect was stored in the database of bad pixel as the event lists were created. A zoom into the source region is shown in Fig. 5.7. Similar to MOS1, the source is located in the middle of the CCD array and can be extracted with 40 arcsec sized source and background regions. The background was extracted in the same y-distance as the source.

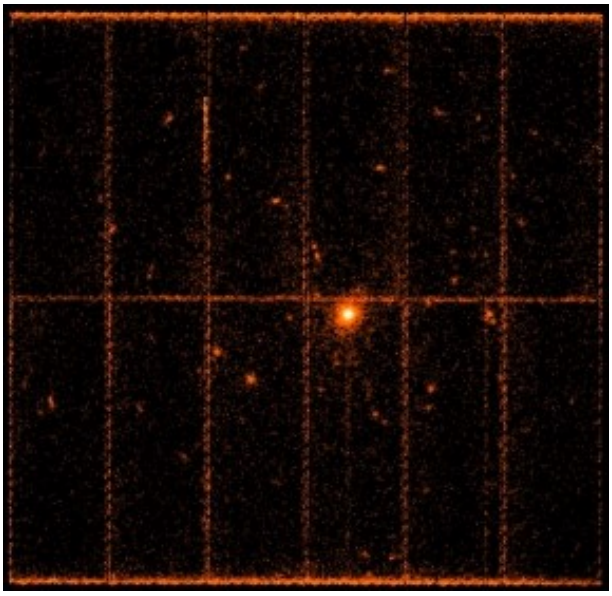

Figure 5.2: Image of the EPIC pn detector with 12 CCDs. NGC 1052 is clearly visible on the forth CCD in the lower row.

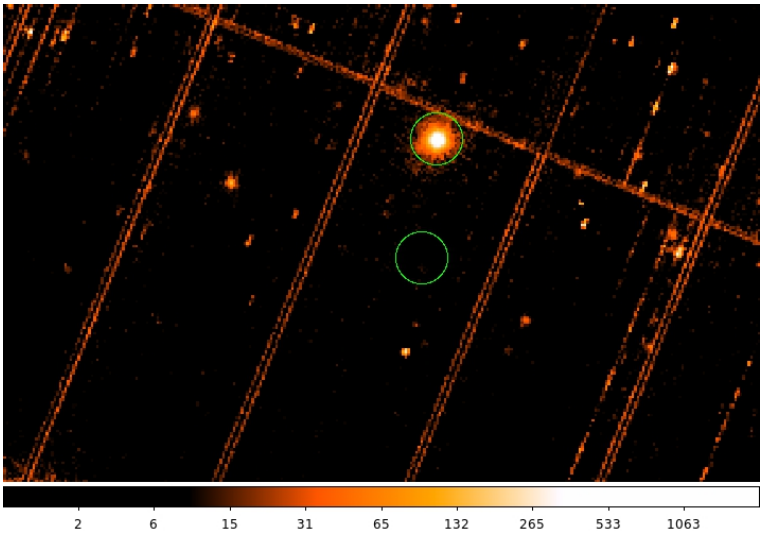

Figure 5.3: A zoom into the source region of NGC 1052 on the pn detector. The green circles represent the selected region of 35' for the source and the background on the same CCD. The brightness of the pixels shows the count rate of photons, which is represented on the x-axis.

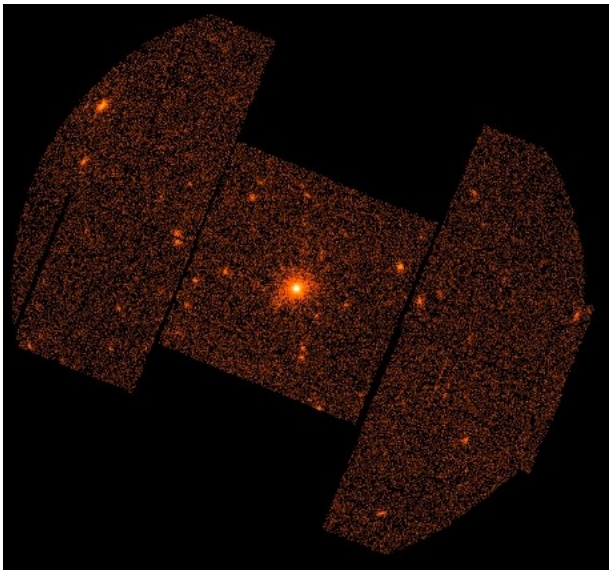

Figure 5.4: Image of the EPIC MOS1 detector with 7 CCDs, with 3 of them not being functional during this analysed observation. NGC 1052 lies in the middle of the centered CCD.

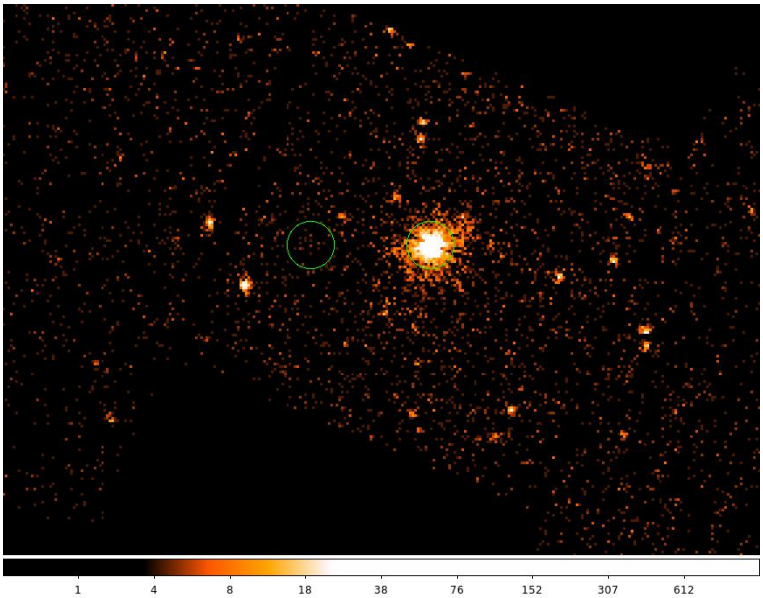

Figure 5.5: A zoom into the source region of NGC 1052 on the MOS1 detector. The green circles represent the selected region of 40' for the source and the background on the same CCD and same y-distance. The brightness of the pixels shows the count rate of photons, which is represented on the x-axis.

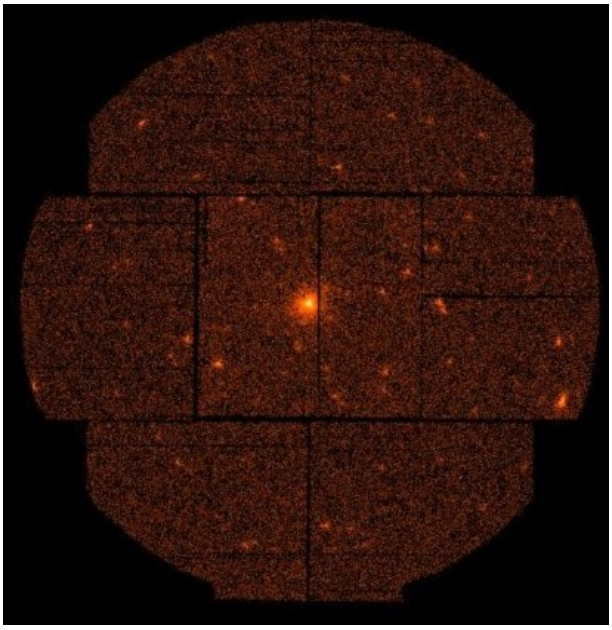

Figure 5.6: Image of the EPIC MOS2 detector with 7 CCDs. NGC 1052 lies in the middle of the centered pixel.

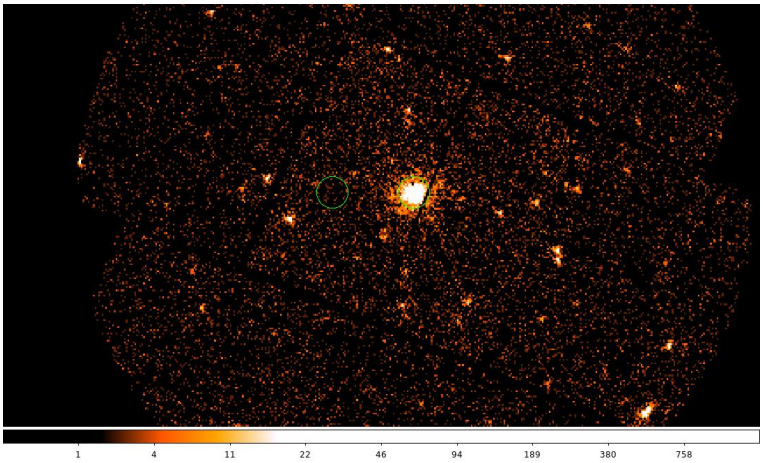

Figure 5.7: A zoom into the source region of NGC 1052 on the MOS2 detector. The green circles represent the selected region of 40' for the source and the background on the same CCD and same y-distance. The brightness of the pixels shows the count rate of photons, which is represented on the x-axis.

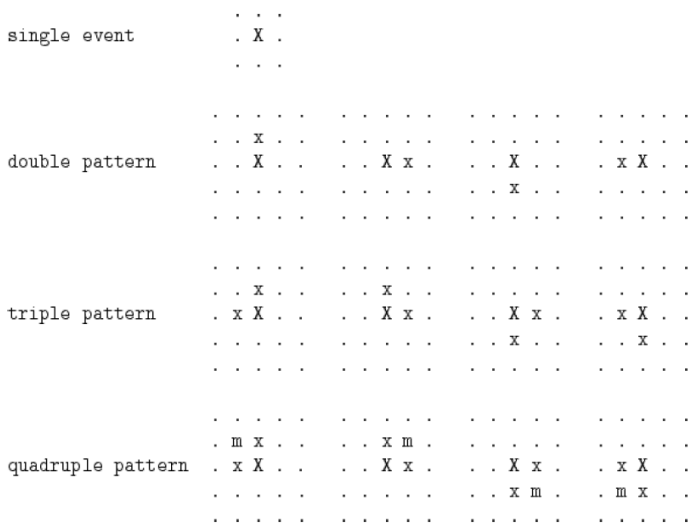

Figure 5.8: Pixel patterns of the EPIC pn camera. 'X' marks pixels with maximum charge, 'x' pixels with medium charge and with 'm' pixels with minimum charge are symbolized. The dots correspond to pixels that did not detect an event. *Credit: (ESA, 2012)*

Another selection criterion was the pixel pattern of the events. Patterns refer to the combination of pixels hit by a photon. Figure 5.8 shows the 13 valid patterns for EPIC PN data. To extract the source spectrum, single and double events were selected from the source region to get the most accurate energy resolution (ESA, 2012). For the MOS detectors all valid patterns are included. The filtered event list are read via *evselect* and the bin size of the spectrum was set to 5 for all EPIC cameras. The maximum of the channels differs for the pn e.g. *specchannelmax=20479* and the MOS e.g. *specchannelmax=11999*. The shortcut FLAG is used to encode various event conditions, e.g. when the source lay near hot pixels or outside the FOV (ESA, 2012). To provide the most conservative screening criteria, *FLAG==0* was set for pn. For the MOS cameras the default parameter values were sufficient. The same conditions were set to extract the spectrum of the background region. In the end, the source and background areas had to be calculated with *backscale* to scale the background region to the source region and take the boundaries and bad pixels of the CCDs into account. Based on the source spectrum the redistribution matrix file (rmf) was created via *rmfgen*, which includes the scattering of events on the detector and response them as a energy function. Additionally the ancillary region file (arf) was created via *arfgen* with generated information about detector properties, like the effective detector area and quantum efficiency. Both files are necessary files, that store the influence of the detector and telescope on the observed spectrum.
With the extraction of the regions of source and background new lightcurves are created for the selected regions on the detector. Since NGC 1052 is an extended source and located at the edge of a CCD at the pn detector, it was checked whether a change in the light curve of the source becomes visible when the extraction area is enlarged, such that more counts from the source lie within the region. Therefore, besides the already mentioned circle region with

35 arcsecond radius, a box region with a size of $A_{box} = 117 \cdot 92$ arcsec was extracted on the pn detector. Figure 5.9 shows the lightcurve of the circle region on the pn detector with the rate of counts per second versus observation time in seconds. The source lightcurve is shown in black and the background lightcurve in red. Both lightcurves are with a bin size of 100 seconds. The detectors image with the selected circular regions is shown above the source lightcurve. The variability in the source lightcurve is visible at the same time in the background lightcurve. The variability is consistent with intervals of high-energetic particle flaring as seen in Fig. 5.1. This indicates that the variations are not source intrinsic but due to a higher background level.

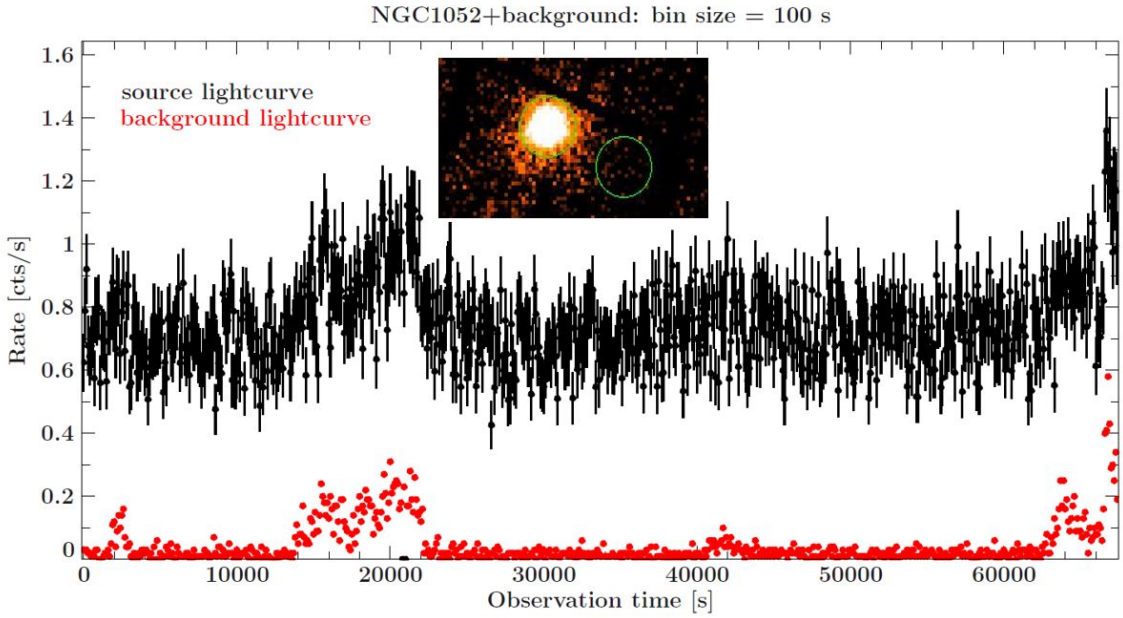

Figure 5.9: Lightcurve of the pn detector with a circle region with a size of $A_{circle} = 3849$ arsec^2.

The same variability in source and background lightcurve is visible for different sizes of the source and background region, as well as for selecting the background region on another region of the detector. In comparison to circular regions, Fig. 5.10 shows the lightcurve of NGC 1052 in black and the background in red with selected box regions and a bin size of 100 seconds. The box regions on the pn detector are displayed in the upper left of the figure. One can see the variability in the lightcurves of source and background at the same time slots as in Fig. 5.9, but with a much higher count rate. The bigger the region size the more photon counts per second are registerd on the detectors area. This indicates, that the rate depends on the size of the selected region. The circle region size is about $A_{circle} = 3849$ arcsec^2 in comparison to the box region with a size of $A_{box} = 10764$ arsec^2.

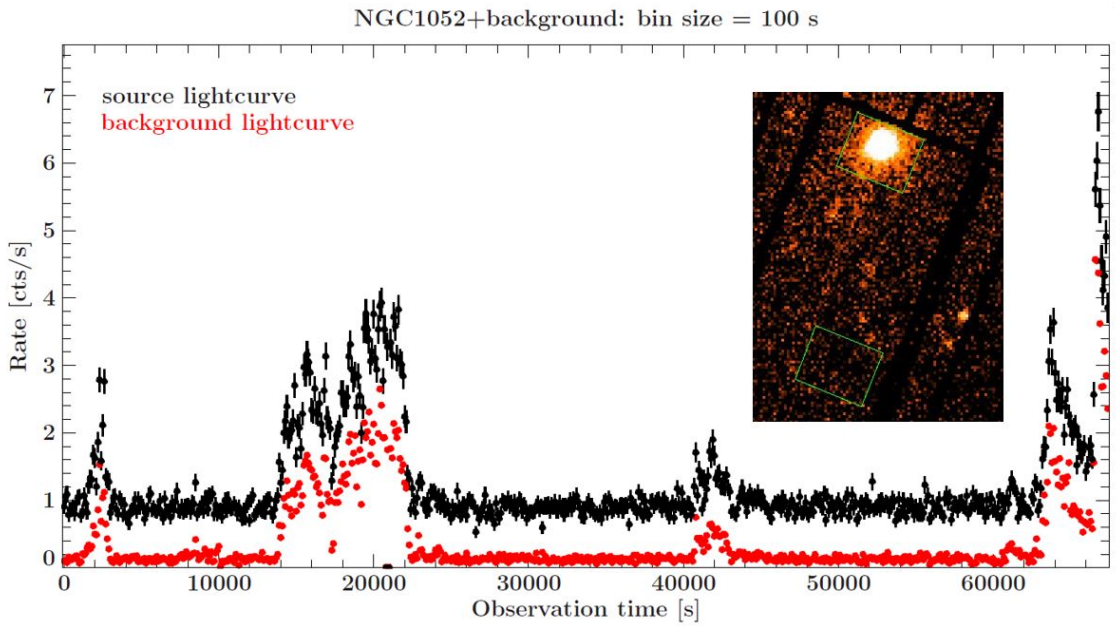

Figure 5.10: Lightcurve of the pn detector with a box region with a size of $A_{box} = 10764$ arsec^2.

Thus, apart from the dependence of the rate on the size of the extraction area, no significant change of the count rate of the light curve is visible if the area size of the source is enlarged. However, the representation of the source light curve and the background light curve in the same figure shows that the background is illuminated by background flares, for example from high-energetic particles, but due to unknown reasons the affected times were not eliminated during the standard extraction. This is also visible in the MOS light curves, even if the count rate is generally smaller and the detector less sensitive due to the smaller effective area. The lightcurve of MOS2 is shown in Fig. 5.12, while the lightcurve for MOS1 looks similar.
Figure 5.11 shows again the source and background light curves of the circle regions including the selected good time intervals by the standard routine (see section 5.2) in grey. The image reveals that almost the entire observation time was selected as a good time interval. Obviously the generated GTI file is wrong, because the flaring from the background is also visible in the source lightcurve. Therefore, a new GTI file was manually created for this observation with the help of these light curves. This was done using *tabgtigen* and the expression for the counts as mentioned in section 5.2. The further analysis of the spectra was done with the new generated GTI file, resulting in a steady light curve for NGC 1052. The background of the generated lightcurves is presumably induced by soft proton flaring.
Figure 5.13 shows the new generated lightcurve for pn, which was performed with the new GTI file. The exclution of the flaring particle background resulted in time gaps, wich can be seen in the lightcurve of NGC 1052. This lightcurve shows no variability of NGC 1052 during this observation.

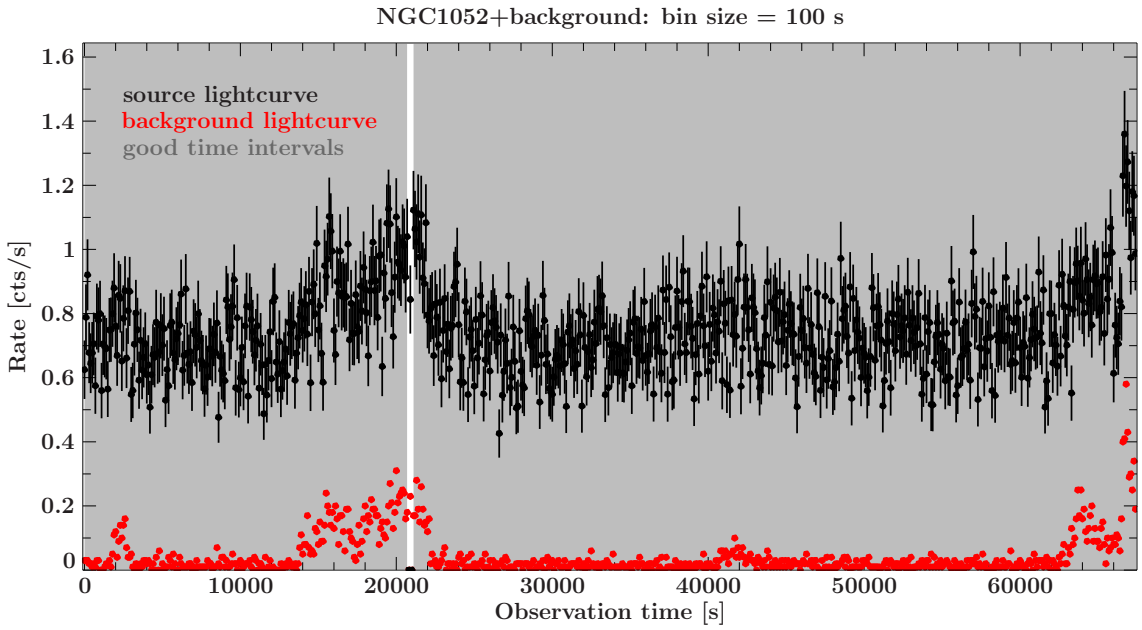

Figure 5.11: Lightcurve of NGC 1052 in black and the background in red with a 100 s bin size of a circle region of 35 arsec from the pn detector. The grey deposited area represents the wrong good time intervals.

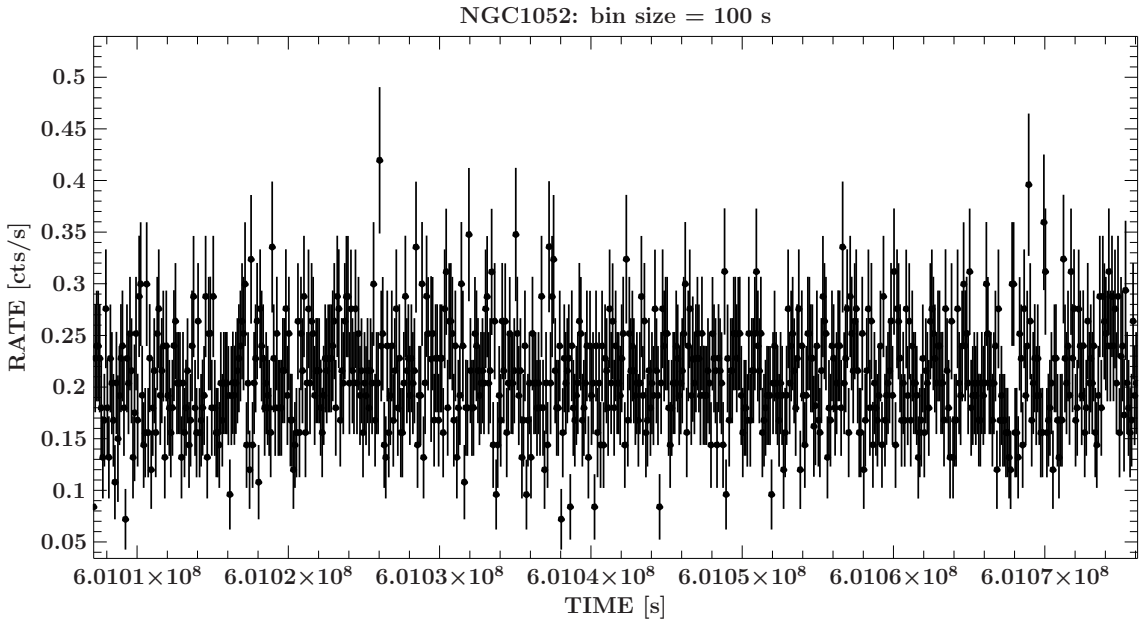

Figure 5.12: Lightcurve of NGC 1052 in black of the MOS2 detector with a 100 s bin size of a circle region of 40 arsec.

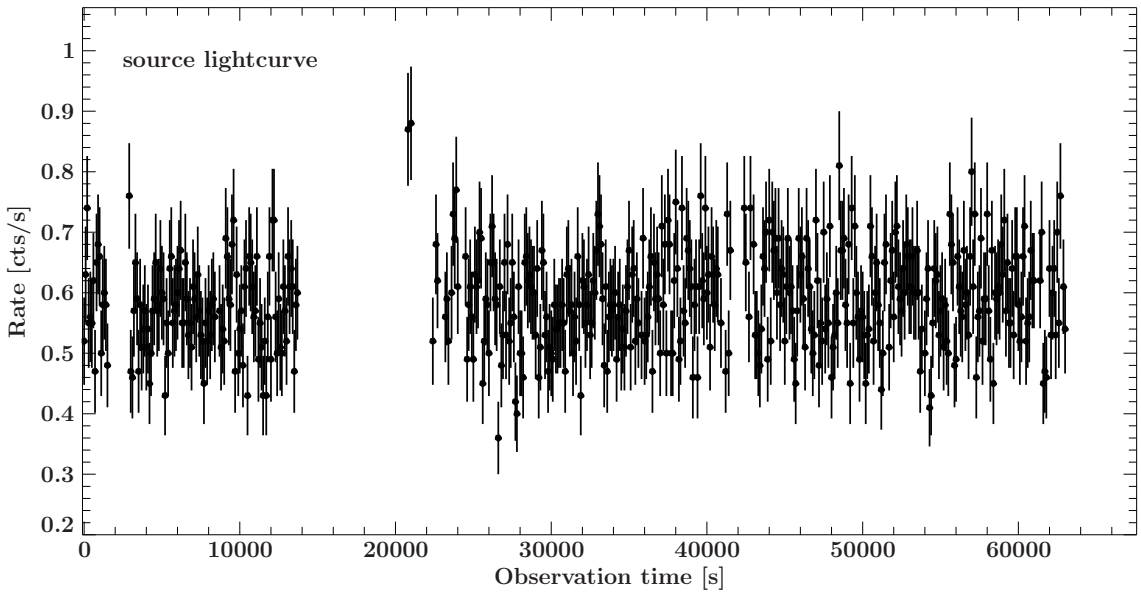

Figure 5.13: Lightcurve of NGC 1052 in black with a 100 s bin size of a circle region of 35 arsec from the pn detector. The gaps are the result of the removement of the flaring background.

6 Analysis of the spectra of NGC 1052

The analysis of the X-ray data was performed using the Interactive Spectral Interpretation System (ISIS) version 1.6.2-43[1] (Houck & Denicola, 2000). First, the dataset from all EPIC detectors was loaded into ISIS, the arf and rmf were assigned and the background was defined. Table 6.1 lists the properties of the data set of the EPIC camera detectors before the spectra were rebinned. *totcts* represents the total number of counts within a spectrum file, consisting of both source and background counts. *nbins* represents the total number of bins and *exp* the exposure time in kiloseconds.

detector	*totcts*	*nbins*	*exp* (ksec)
pn	2.7817×10^4	4096	43.611
MOS1	8.2980×10^3	2400	49.343
MOS2	8.7610×10^3	2400	49.400

Table 6.1: The properties of the spectra of the EPIC camera, where *totcts* means the total number of counts, *nbins* the total number of bins, and *exp* the exposure time in kiloseconds.

6.1 Rebinning the spectrum

Rebinning or grouping of data gives a better statistical measure of the source counts (Arnaud et al., 2011) as this increases the number of counts per bin. Since a pixel of a CCD camera can either experience the detection of a photon or no detection, the resulting values are distributed according to Poisson. In order to use χ^2 statistics, normally distributed data is needed. Poisson distribution is approaching a normal distribution for a large number of counts. As a rule of thumb, 30 data counts per energy bin are required to apply χ^2 statistics (Gehrels, 1986). Based on the energy resolution of the instruments, the events are typically binned into detector energy channels.
The signal-to-noise ratio (SNR) describes how significant the source signal is compared to the background noise and should be as large as possible. One way to rebin the data is a combination of a required minimal value for the SNR and a minimal number of channels in each grouped bin. Using the ISIS command *group*, the background is included in this SNR calculation, while a simple rebinning method *rebin_data* does not take the counts of the background into account. Using that technique, the energy channels are rebinned such that each new bin contains at least 30 counts. As shown in Table 6.1, the total counts for pn and MOS are different for this observation due to a smaller effective area for MOS. Therefore, the SNR is chosen differently

[1] ISIS Software (https://space.mit.edu/cxc/isis/, March 24, 2019)

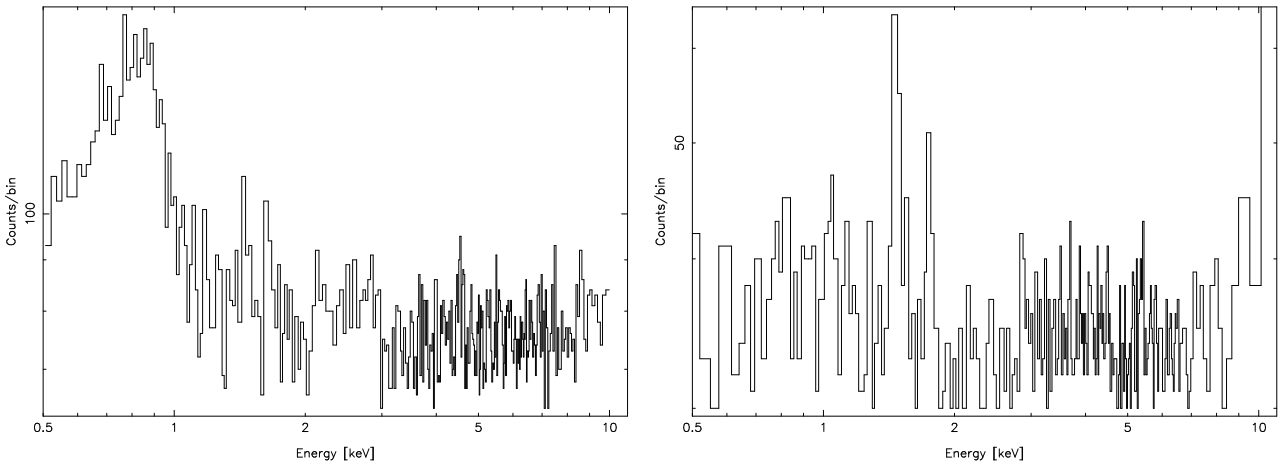

Figure 6.1: Number of counts per energy bin for pn (*left panel*) and MOS2 (*left panel*) after grouping. For pn a SNR ≥ 8 is required for each energy bin, while the MOS2 spectrum is with SNR ≥ 5.4.

for the detectors. Figure 6.2 shows the MOS1 spectrum rebinned to 30 counts per bin. Due to a low signal to noise ratio, MOS1 was not used for further spectral analysis.
For pn and MOS2 the spectra were rebinned to yield a minimum SNR of 8 and 5.4 for each bin, respectively. The resulting number of counts per energy bin are shown in Fig. 6.1.

Due to the rebinning/grouping process, the total number of bin decreased. In Table 6.2 the number of bins for each detector after the binning is listed.

detector	*nbins*	*method*
pn	326	*group*, SNR>= 8
MOS1	252	*rebin_data*, counts>= 30
MOS2	247	*group*, SNR>= 5.4

Table 6.2: Properties of the spectra of the EPIC camera after rebinning the spectrum with the used method for rebinning. *nbins* is the total number of bins.

6.2 Model fitting

Due to the functionality of CCD cameras it is not possible to measure the source spectrum directly. The source flux is not measured in terms of the energy $f(E)$, but as numbers of photons $N(C_i)$ per integrated time bins within an instrument channel C_i of the CCD camera, given as

$$N(C_i) = B_i + t_{exp} \int R(C_i, E) A_i f_i(E) dE, \tag{6.2.1}$$

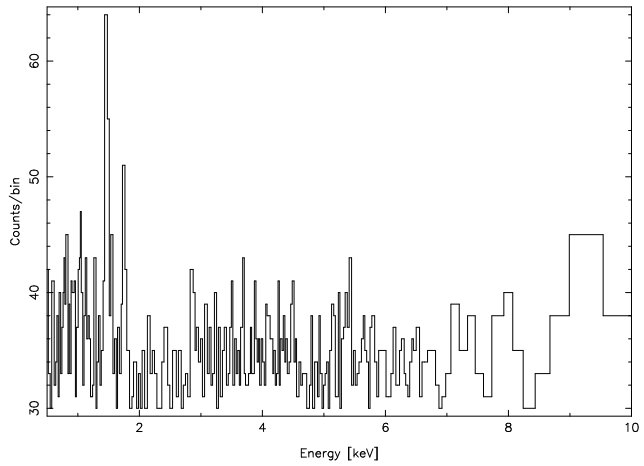

Figure 6.2: Number of counts in the MOS1 spectrum after rebinning to a minimum of 30 total counts per energy bin.

where B_i is the background contribution in the detector channels. The quantity $R(C_i, E)$ is called redistribution matrix function (rmf), which is the probability of a photon of the energy E is measured in the channel C_i. A_i is the ancillary region file (arf).
The aim is to find a model which fits best to the data, meaning that the model parameters describe the underlying physics properly where the χ^2 has a global minimum. During the process of adapting the model to the data, counts are calculated for each bin for a given set of parameters and are then compared to the counts of the spectrum. For this, the χ^2-statistic is used, where the photon events X_i per energy interval i are subject to a Gaussian distribution, and described by the following probability function:

$$\chi^2 = \sum_{i=1}^{N} \frac{(X_i - M_i)^2}{M_i}, \tag{6.2.2}$$

where M_i represents the expected events given by the model and X_i is used to test how well the model describes the data, called goodness-of-fit (Arnaud et al., 2011).
A model is a theoretical description of the intensity as a function of energy based on assumptions on the physical processes that take place within the X-ray source. The task is to find a combination of parameters such that the deviation between the model and the data is minimized. The goodness of such a fit is measured with a test statistic, typically χ^2 statistic. The model spectrum calculated the expected number of counts per bin given a theoretical assumption. Therefore, the χ^2 test statistics sums up the difference between the expected and observed counts per bin taking into account the statistical fluctuation. Any minimum of the χ^2 will result in a local minimum. That is why a good measurement of the goodness-of-fit is the reduced χ^2, expressed by this formula:

$$\chi^2_{red} = \frac{\chi^2}{\nu}, \tag{6.2.3}$$

where ν represents the number of parameters minus the degrees of freedom $d.o.f.$. A good model fit should get the value of $\chi^2_{red} \approx 1$ (Arnaud et al., 2011). To find the best spectral fit

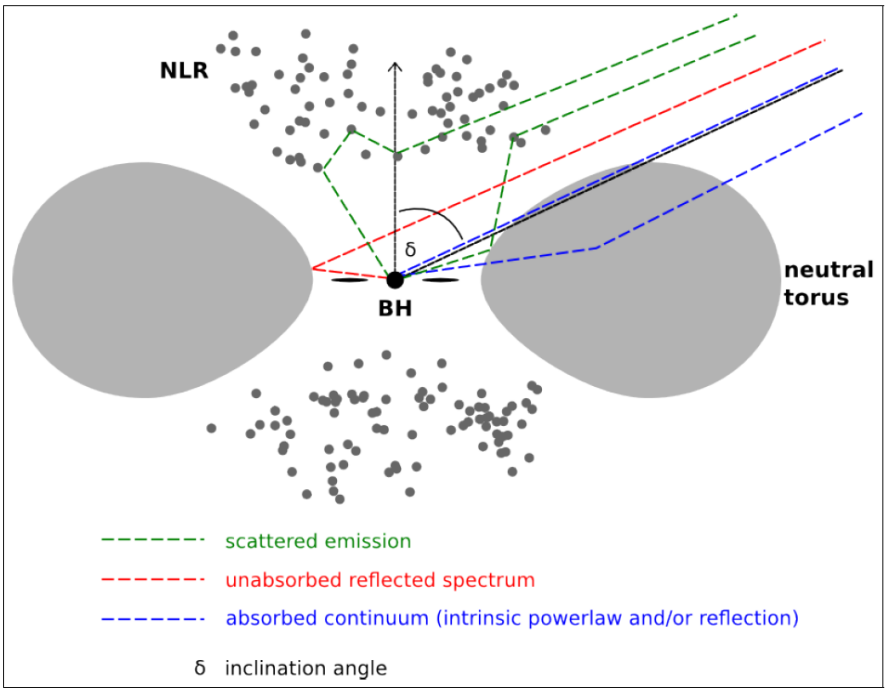

Figure 6.3: Possible components of an X-ray spectrum and their origin are sketched. Continuum components are the absorbed continuum (blue dashed line) as seen through the torus and the reflected unabsorbed spectrum (red dashed line), which can consist of a complex of emission lines, i.e. iron, due to fluorescence. Another scattered component from the NLR is considered ionized reflection lines (green dashed line). *Credit: R. Schulz*

to the data, several models were tested in this work.

6.3 Models

This section is intended to give a brief introduction to the theoretical models used in this work, which describe processes in AGN that cause emission in the soft X-ray range (0.5 - 10 keV). Figure 6.3 shows an AGN and possible interactions of the photons before they can be observed by an observer. The photons resulting from the accretion disk of the AGN, can either get absorbed or reflected at the torus, scattered at the NLR or BLR of the AGN or a combination of all these processes. For NGC 1052 the the inclination angle is large, which means that we observe the system edge-on, so that the accretion disk and the black hole are covered by the torus. The observed flux, as well as the shape of the X-ray spectrum, is influenced by the optical depth of the obscuring torus.

Most of the following models are taken from the Xspec Manual[2], where all common models for spectral fitting are listed.

[2]Summary of Models (https://heasarc.nasa.gov/xanadu/xspec/xspec11/manual/node38.html, March 20, 2019)

powerlaw: An intrinsic X-ray emission of AGN, resulting from inverse Compton scattering of thermal radiation at higher energies, e.g. from the accretion disk. The describing parameter is the photon index Γ of the power law in terms of photons/keV/cm^2/s at 1 keV.

apec: A thermal plasma model of an emission spectrum of collisionally ionized diffuse gas. This model associates soft X-ray emission with emission lines of ionized elements within the thin, highly ionized NLR. These are irradiated by the original continuum from the central region, leading to the formation of many emission lines. The model is described by the parameter z for the redshift of the source, kT for the plasma temperature in keV and *Abundance* for the metal abundances, including the elements Mg, Al, Si, Fe, Ni.

zgauss: A redshifted gaussian profile. Parameters are the line energy *LineE* in keV, the line width σ in keV and the reshift z of the source. If the $\sigma = 0$, then the emission line is treated as a delta function. The absorption of X-rays leads to the excitation and ionization of K- and L-shells of neutral elements. The stimulated electrons return to their ground state and cause an emission line in the observed spectrum due to fluorescence. The central region of an AGN has a high iron abundance, which makes the emission lines of this element a prominent property of many AGN spectra.

bremss: A thermal bremsstrahlung spectrum based on Kellogg et al. (1975), described by a plasma temperature kT in keV as parameter.

tb_new_simple: A photo absorption model of X-ray photons in the interstellar medium by Jörn Wilms[3]. The describing model parameter is the hydrogen column density N_H. Two absorption models are taken into account: absorption within the Milky Way, where N_H is fixed to the Galactic value in the direction of the source, and a source intrinsic absorption, e.g., by the torus, where N_H is left free to vary.

relxill: A Compton reflection model by Thomas Dauser[4], base on a combination of the reflection code xillver (García et al., 2013) and the ray tracing code relline for a relativistically broadened emission line (Dauser et al., 2013). The parameters of this model are:

- a: the spin of the black hole.
- *Incl*: the angle between the line of sight and the normal of the reflecting medium. Assuming Compton reflection off the inner accretion disk, the angle is similar to the inclination angle of the source.
- $refl\_frac$: the reflection fraction describing the ratio of the coronal intensity illuminating the disk to the coronal intensity, which reaches the observer (Dauser et al., 2016a).
- R_{in} and R_{out} as the inner and outer radius of the accretion disk.

[3] Jörn Wilms (http://pulsar.sternwarte.uni-erlangen.de/wilms/research/tbabs/, March 24, 2019)
[4] Thomas Dauser (http://www.sternwarte.uni-erlangen.de/~dauser/research/relxill/index.html, March 24, 2019)

- $Index1$, $Index2$: emissivity indices for the coronal models, which can be modeled using a power law (only one Index) or a broken power law (the intensity on the disk $I \propto r^{-Index1}$ with $R_{in} < r < R_{br}$ and $I \propto r^{-Index2}$ with $R_{br} < r < R_{out}$; R_{br} represents the breaking radius) (Abdikamalov et al., 2019).
- $logxi$: the ionization of the accretion disk, ranging from 0 (neutral) to 4.7 (heavily ionized).
- A_{Fe}: the iron abundance of the material in the accretion disk.
- Γ: photon index.
- z: redshift of the source.
- E_{cut}: high energy cutoff of the primary spectrum.

6.4 Results

In the following two different models, which both describe the spectrum of NGC 1052 well, will be explained and compared afterwards. If not mentioned otherwise, only the pn spectrum was used for the spectral analysis. For all models, the parameter redshift was fixed to z=0.005, which was taken from the NASA Extragalactic Database (NED)[5].

6.4.1 Partial covering model

Based on earlier studies of NGC 1052 from Boeck (2012), a partial covering scenario was a good starting point for a fit to the X-ray source spectrum. In a partial covering model it is assumed that one part of the original power law is absorbed by the torus and the other part can reach the observer without interference due to an inhomogeneous structure of the torus. Photon absorption has no effect in the hard energy regime and it only affects the soft regime. The soft power law is caused by the scattered or reflected continuum at the torus. In this thesis, this complex model was fitted using a soft power law and an absorbed power law component. They have the same origin and thus the same photon index. The complete model was defined as:

$$tb\_new\_simple_{gal} * (apec_1 + zgauss_2 + powerlaw_1 + tb\_new\_simple_{intr} * (powerlaw_2 + zgauss_1)), \tag{6.4.1}$$

where $tb\_new\_simple_{gal}$ describes the Galactic absorption and thus affects the whole model. Extended emission from the host galaxy is considered by Boeck (2012) with the plasma model $apec_1$. The multiplicative intrinsic absorption of hydrogen $tb\_new\_simple_{intr}$ affects the unabsorbed part of the power law. This model includes a narrow fluorescence line Fe Kα at an energy of about 6.4 keV. The emission line of iron is expected to come from an interaction of X-rays with the surrounding material. Additional an emission line of Si Kα at an energy about 1.8 keV was suggested. The model fails to reproduce the accurate postion of the Si line at 1.8keV, which is reflected in the large error range of this parameter (see Table 6.3.

[5]NASA/IPAV Extragalactic Database (https://ned.ipac.caltech.edu/, March 24, 2019)

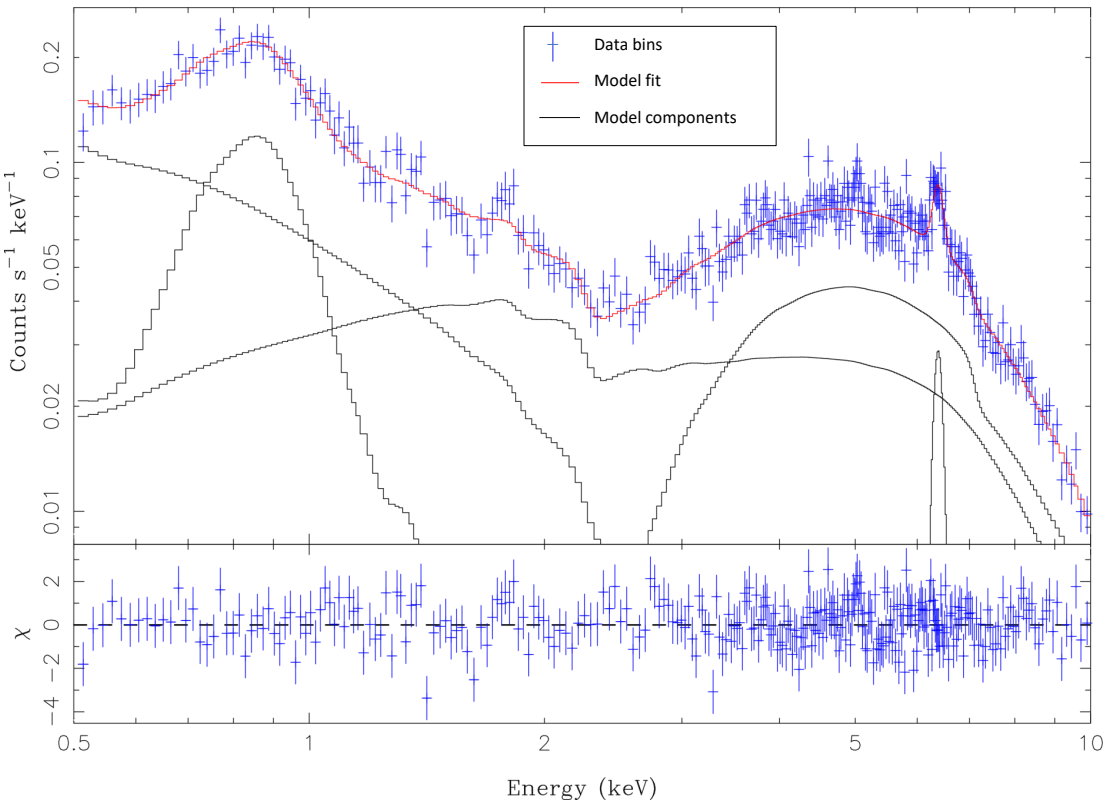

Figure 6.4: Fit to the spectrum of NGC 1052. The top panel shows the complete model fit in red with the components in black and the data bins in blue. The residuals are shown in the bottom panel.

The best fit of this model to the spectrum is shown in Fig. 6.4. The spectrum respresents the photon counts per second and keV in dependence of the energy in blue, with both axes in logaritmic scale. In red is the complete model and in black are the shapes of all model components. The residuals, shown in the bottom panel, give an indication of how well the model describes the spectrum.
Further, the *Abundance* of the apec was fixed to to the solar abundance. All the parameters of the fit are listed in Table 6.3 below. This model fit resulted in $\chi^2/d.o.f.$ (χ^2_{red}) = 295.65/287 (1.03).

6.4.2 Spectrum fit with relxill

On the basis of the analysis from Brenneman et al. (2009), where a relativistically broadened iron line was suggested, a Compton reflection model was used. This alternative model was implemented with relxill. The complete model is described by the following:

$$tb\_new\_simple_{intr} * relxill + bremss + apec_1 + apec_2 + zgauss_1 + zgauss_2. \tag{6.4.2}$$

Parameter	Value	Unit
$N_{H,intrinsic}$	17^{+8}_{-4}	$[10^{22}\ \mathrm{cm}^{-2}]$
Γ	$1.9^{+1.2}_{-0.6}$	
$norm_{powerlaw,1}$	$5.6^{+2.4}_{-1.8}$	$[10^{-5}]$
$norm_{powerlaw,2}$	2.0	$[10^{-3}]$
$N_{H,galactic}$	≤ 0.11	$[10^{22}\ \mathrm{cm}^{-2}]$
$apec_{1,norm}$	$2.30^{\dagger}$	$[10^{-5}]$
$apec_{1,abun}$	1^{*}	
kT_{apec_1}	$0.80^{+0.04}_{-0.05}$	[keV]
$E_{FeK\alpha}$	$6.413^{+0.023}_{-0.038}$	[keV]
$\sigma_{FeK\alpha}$	0.001^{*}	[keV]
$norm_{FeK\alpha}$	$1.34^{+0.35}_{-0.29}$	$[10^{-5}]$
$E_{SiK\alpha}$	$3.8^{+1.3}_{-3.9}$	[keV]
$\sigma_{SiK\alpha}$	$4.7^{+4.4}_{-2.2}$	[keV]
$norm_{SiK\alpha}$	$4.1^{+5.1}_{-2.8}$	$[10^{-4}]$
χ^2/d.o.f.	295.65/287	

Table 6.3: Best fit parameters for the partial coverer fit of the X-ray continuum and the emission lines with the calculated errors. Parameters indicated with a $*$ have been frozen during the fitting process. The † signifies a parameter whose error calculation did not converge.

Instead of a partial coverer model, an additional apec and a bremss model were used to fit the soft energy band. The reflection model relxill describes the spectrum at higher energies. The spectrum with components is shown in Fig. 6.5, while the free parameters are listed in Table 6.4. The accretion disk is presumably located in the equatorial plane of the black hole and extends from an outer radius R_{out} to an inner radius R_{in}, which is generally at or near the innermost stable circular orbit (ISCO) of the black hole. In this model fit it was assumed that a normal power law distribution is given. For the emissivity, a normal power is assumed. Thus, after a first fit of the parameters $Index1 = Index2 = 3$ were tied and freezed and the outer radius of the accretion disk was tied to the breaking radius to $R_{out} = R_{br} = 135.6$ in gravitational radii. The inner radius was fixed to the value $R_{in} = -1$ in units of the ISCO after the first fit. Assuming a maximally spinning black hole, the spin parameter a was set to $a = 0.99$ and frozen to this value. Also of the high energy cutoff of the primary power law, which allows to constrain the accretion geometry (Dauser et al., 2016b), was fixed to $E_{cut} = 300$ keV after the first fit. The inclination ancle of the accretion disk to the normal of the system was fixed to the upper limit of $Incl = 80°$, basing on VLBI data from NGC 1052 the angle of the jet to the line of sight was determined by Baczko et al. (2016) to be $\approx 86°$. The resulting parameters are in general compatible with their physical statements and already excisting fit parameter, e.g. by Boeck (2012), Kadler et al. (2004) and Brenneman et al. (2009). The complexity of the model did not allow to constrain all fit parameters further, leading to

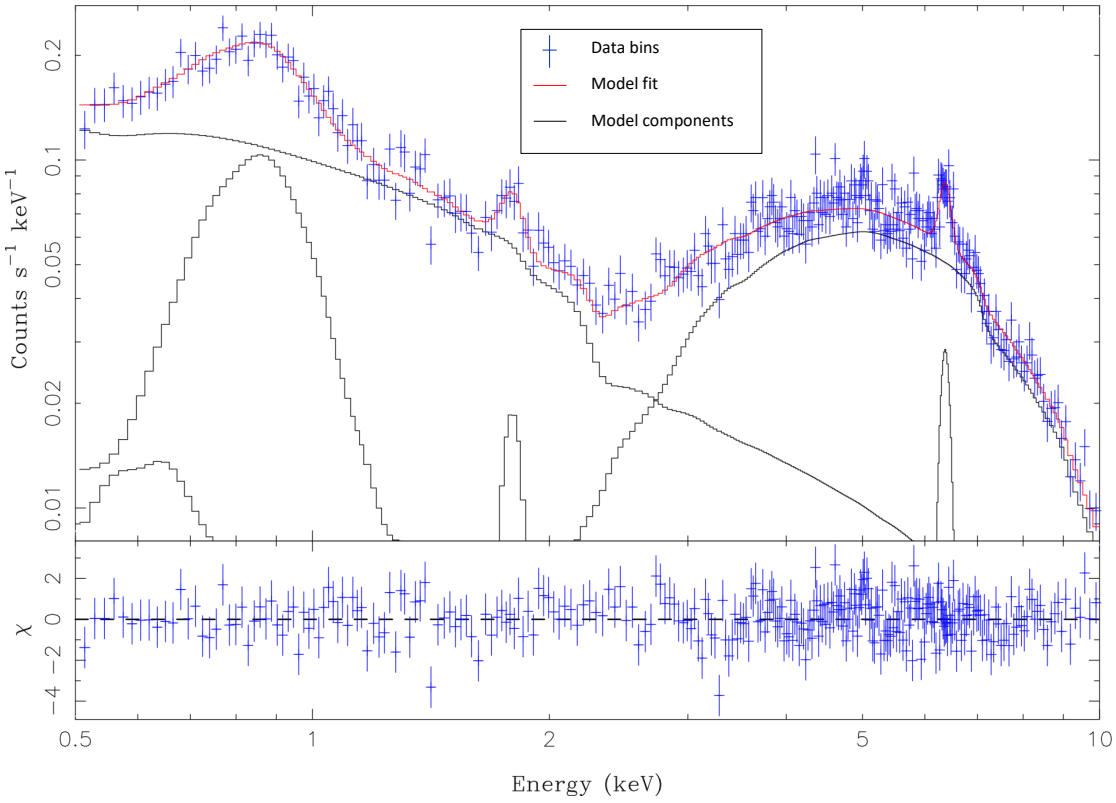

Figure 6.5: Fit to the spectrum of NGC 1052. The top panel shows the complete model fit in red with the components in black and the data bins in blue. The residuals are shown in the bottom panel.

large errors, which can indicate correlations between some parameters. This model fit resulted in $\chi^2/d.o.f.$ $(\chi^2_{red}) = 291.82/277$ (1.05).

Residual emission at 5 keV

A closer look at the two models fits reveals residual emission at 5 keV. To check whether a line fit at this energy has an impact to the goodness of the fit, an additional line ($zgauss_3$) was included in the previous model:

$$tb\_new\_simple_{intr} * relxill + bremss + apec_1 + apec_2 + zgauss_1 + zgauss_2 + zgauss_3. \tag{6.4.3}$$

Basing on the Fig. 6.6 from Dauser (2010), a relativistic broadened iron line with additional feature at around 5 keV is assumably. The graphic shows the variations of the model components for changing parameters of the inclination angle and the emissivity index. For larger values of the emissivity index, more photons emerge from the highly relativistic inner regions of the accretion disk (Dauser, 2010).
The spectrum with additional emission line is shown in Fig. 6.7 and the parameters of the fit

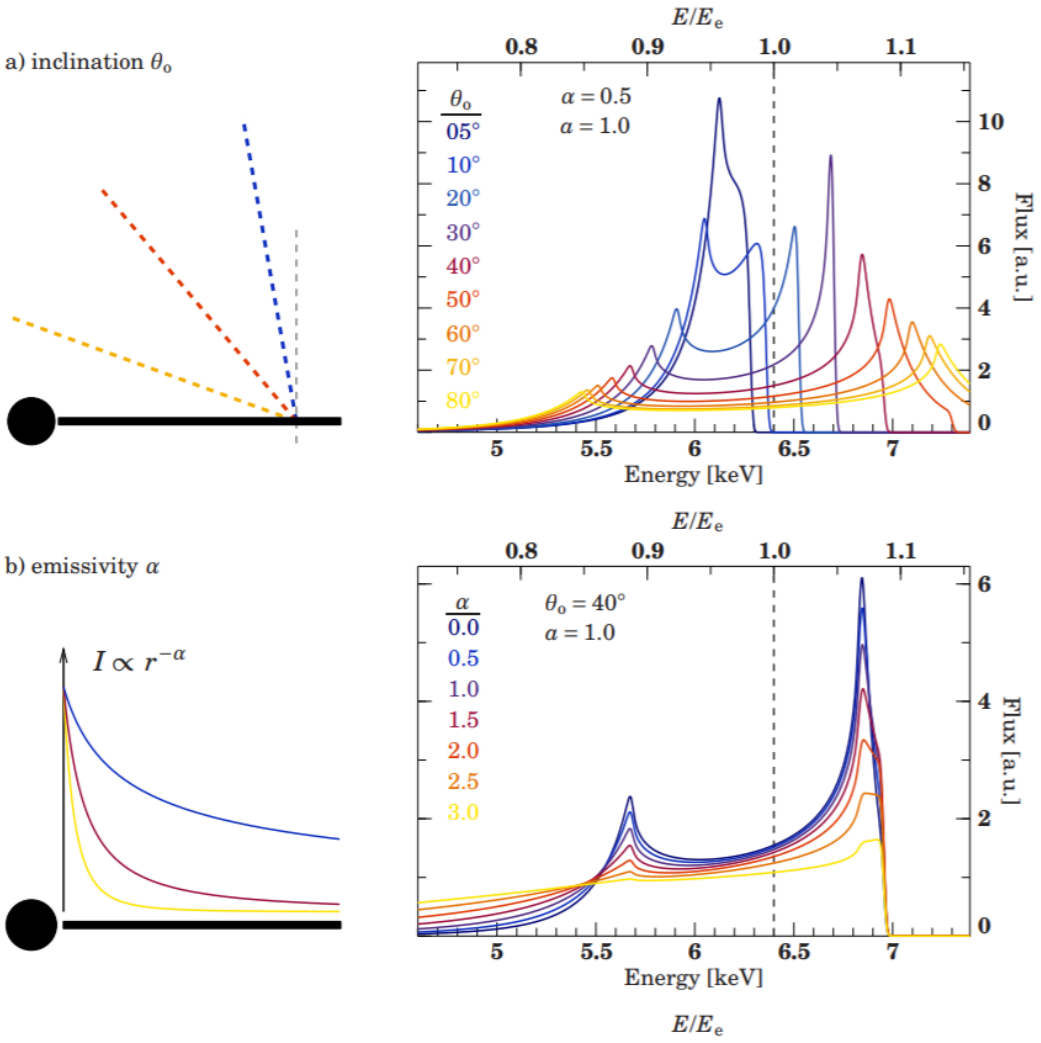

Figure 6.6: The shape of broad lines for different a) inclinations Θ, b) emissivity indices α. *Credit: (Dauser, 2010)*

Parameter	Value	Unit
$N_{H,intrinsic}$	$12.4^{+1.3}_{-1.2}$	$[10^{22}\ \mathrm{cm}^{-2}]$
$norm_{relxill}$	$1.01^{\dagger}$	$[10^{-5}]$
$Index1_{relxill}$	3^{*}	
$a_{relxill}$	0.99^{*}	
$Incl_{relxill}$	80^{*}	$[deg]$
$Rin_{relxill}$	-1^{*}	
$Rout_{relxill}$	135.58^{*}	
$\Gamma_{relxill}$	$2.0^{+0.0}_{-0.8}$	
$Ecut_{relxill}$	9.63	
$logxi_{relxill}$	$1.30^{+0.08}_{-1.31}$	
$Afe_{relxill}$	$0.50^{+0.21}_{-0.00}$	
$refl\_frac_{relxill}$	$8.4^{+1.6}_{-6.4}$	
$norm_{bremss}$	$2.30^{+0.10}_{-0.68}$	$[10^{-4}]$
kT_{bremss}	$1.00^{+0.00}_{-0.75}$	$[10^{2}\ \mathrm{keV}]$
$apec_{1,norm}$	$4.17^{\dagger}$	$[10^{-6}]$
kT_{apec_1}	$0.80^{+63.21}_{-0.05}$	[keV]
$apec_{1,abun}$	5^{+0}_{-5}	
$apec_{2,norm}$	$7.76^{\dagger}$	$[10^{-7}]$
kT_{apec_2}	$0.24^{+63.76}_{-0.24}$	[keV]
$apec_{2,abun}$	5^{+0}_{-5}	
$E_{FeK\alpha}$	6.400 ± 0.027	[keV]
$\sigma_{FeK\alpha}$	$0.029^{+0.058}_{-0.030}$	[keV]
$norm_{FeK\alpha}$	$1.01^{+0.25}_{-0.22}$	$[10^{-5}]$
$E_{SiK\alpha}$	1.803 ± 0.029	[keV]
$\sigma_{SiK\alpha}$	$2.57^{\dagger}$	$[10^{-8}\mathrm{keV}]$
$norm_{SiK\alpha}$	2.2 ± 1.0	$[10^{-6}]$
χ^2/d.o.f.	291.82/277	

Table 6.4: Best fit parameters for the relxill model fit of the X-ray continuum and the emission lines with the calculated errors. Parameters indicated with a $*$ have been frozen during the fitting process. The † signifies a parameter whose error calculation did not converge.

are listed in Table 6.5.
However, there is no evidence of an element transition in this energy range that contributes to the physical description of the source. Relativistically broadend iron lines have been found in AGN, althogh a relativistically broadened iron emission line has not been seen in radio-

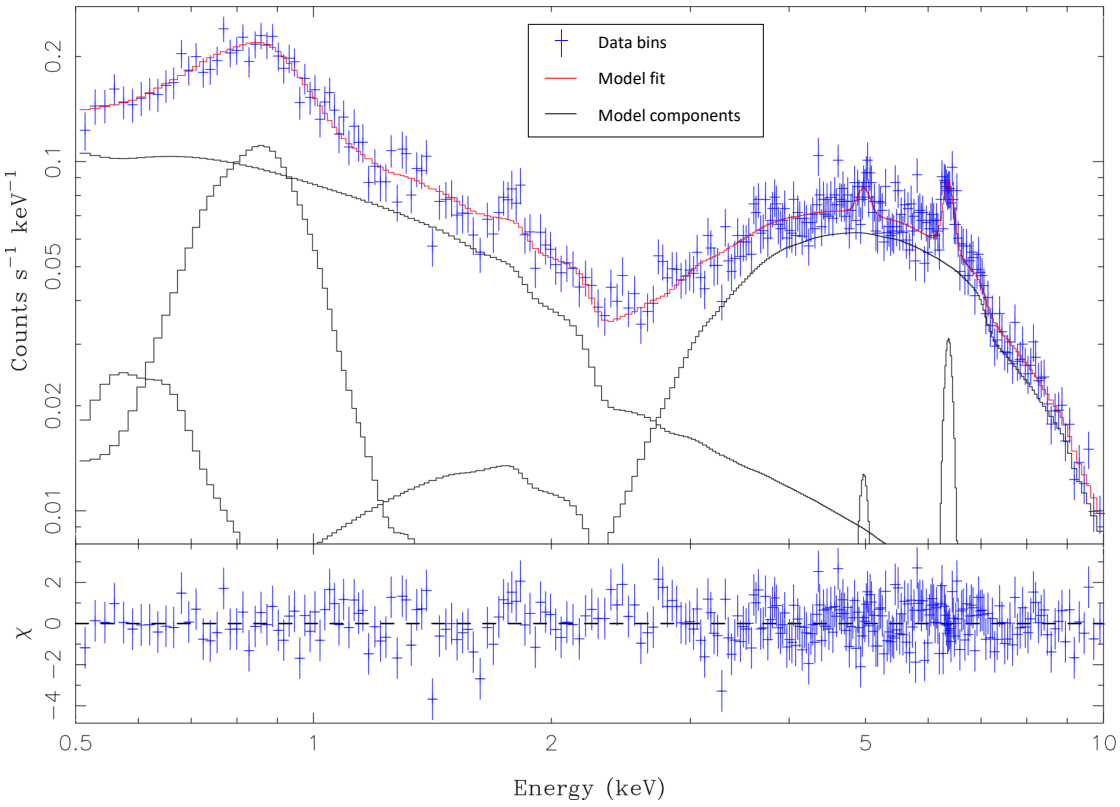

Figure 6.7: Reflection model plus additional line at 5 keV. The top panel shows the complete model fit in red with the components in black and the data points in blue. The residuals are shown in the bottom panel.

loud AGN so far (Boeck, 2012). NGC 1052 shows strong $FeK\alpha$ emission which allows to test for such a component. This model fit with additional emission line at 5 keV resulted in $\chi^2/d.o.f.$ $(\chi^2_{red}) = 275.29/280$ (0.98). The $\chi^2_{red} < 1$, which means that the uncertainties of the fit are overestimated.

To improve the SNR and test for possible line nature of the residuals at 5 keV, the MOS2 data was included in the following analysis. The spectrum of the MOS2 detector was plotted in addition to the spectrum of the pn detector in Fig. 6.8. To take into account different effective areas of the detectors, two detector constants were used. The constant for the pn data was fixed to 1, while the one for the MOS2 data was left free to vary. This resulted in a factor of 1.02 for MOS2, which is a reasonable value since the the different effective areas are considered in the detector RMFs.

In the spectrum of MOS2 of Fig. 6.8 no significant line at 5 keV is visible. This can result result from the smaller effective area of the MOS detectors. The combined model fit with additional emission line at 5 keV and pn with MOS2 together, resulted in $\chi^2/d.o.f.$ $(\chi^2_{red}) = 528.12/515$ (1.03).

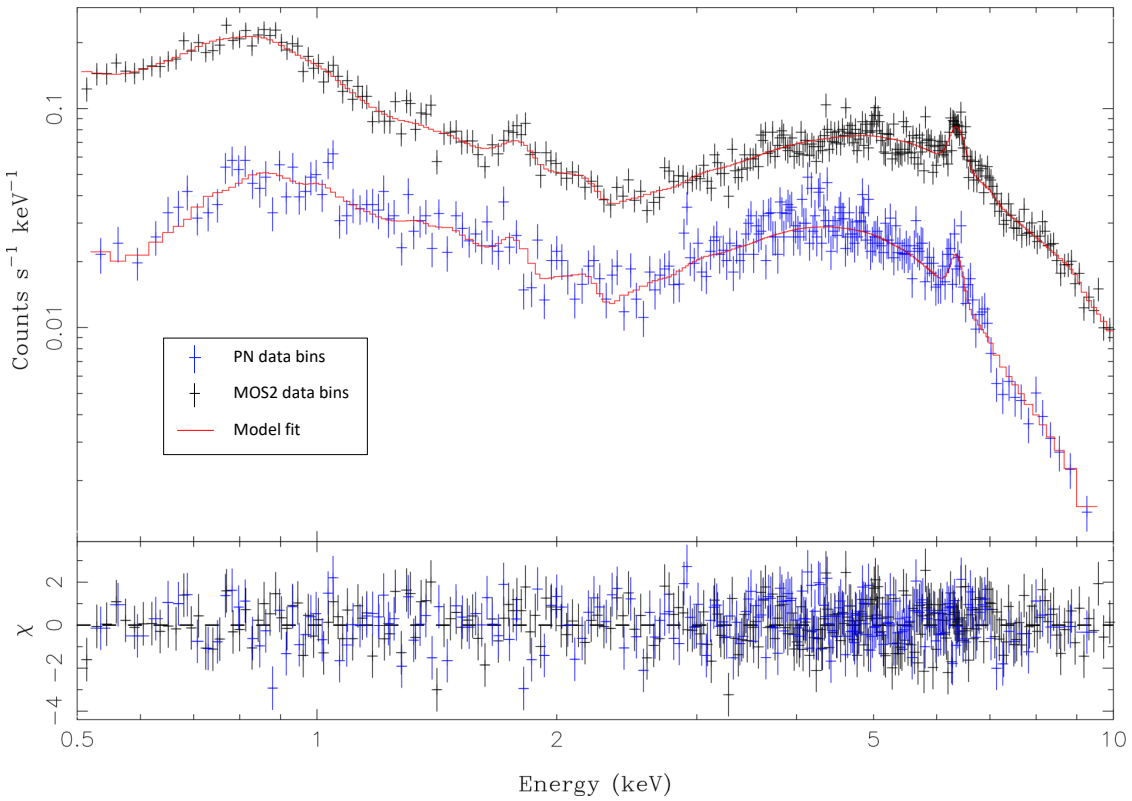

Figure 6.8: Reflection model with additional line emission at 5 keV for pn and MOS2 data. The top panel shows the complete model fit in red with the data bins from the pn detector in black and the data bins from the MOS2 detector in blue. The residuals are shown in the bottom panel.

Parameter	Value	Unit
$N_{H,intrinsic}$	$7.9^{+2.1}_{-1.7}$	$[10^{22}\ \mathrm{cm}^{-2}]$
$norm_{relxill}$	$8.78^{\dagger}$	$[10^{-6}]$
$Index1_{relxill}$	3^{*}	
$a_{relxill}$	0.99^{*}	
$Incl_{relxill}$	80^{*}	$[deg]$
$Rin_{relxill}$	-1^{*}	
$Rout_{relxill}$	135.58^{*}	
$\Gamma_{relxill}$	$2.0^{+0.0}_{-0.8}$	
$Ecut_{relxill}$	300^{*}	
$logxi_{relxill}$	≤ 2.4	
$Afe_{relxill}$	$0.54^{+2.17}_{-0.04}$	
$refl\_frac_{relxill}$	6^{+5}_{-6}	
$norm_{bremss}$	0.0002^{*}	
kT_{bremss}	95^{+5}_{-36}	[keV]
$apec_{1,norm}$	$1.6^{\dagger}$	$[10^{-6}]$
kT_{apec_1}	$0.8^{+63.3}_{-0.8}$	[keV]
$apec_{1,abun}$	$0.27^{+4.74}_{-0.27}$	
$apec_{2,norm}$	$1.6^{\dagger}$	$[10^{-6}]$
kT_{apec_2}	$1.5^{+62.6}_{-1.5}$	[keV]
$apec_{2,abun}$	5^{+0}_{-5}	
$E_{FeK\alpha}$	6.39^{*}	[keV]
$\sigma_{FeK\alpha}$	0.05 ± 0.06	[keV]
$norm_{FeK\alpha}$	$1.13^{+0.34}_{-0.28}$	$[10^{-5}]$
$E_{SiK\alpha}$	1.8^{*}	[keV]
$\sigma_{SiK\alpha}$	≤ 0.07	[keV]
$norm_{SiK\alpha}$	2.3 ± 1.0	$[10^{-6}]$
$E_{5\,keV}$	5^{*}	[keV]
$\sigma_{5\,keV}$	1.2 ± 0.4	[keV]
$norm_{5\,keV}$	9^{+6}_{-4}	$[10^{-5}]$
χ^2/d.o.f.	275.29/280	

Table 6.5: Best fit parameters for the relxill model fit of the X-ray spectrum with an additional emission line at 5 keV with the calculated errors. Parameters indicated with a $*$ have been frozen during the fitting process. The † signifies a parameter whose error calculation did not converge.

Parameter	Value	Unit
$N_{H,intrinsic}$	$7.8^{+10.4}_{-1.8}$	$[10^{22}\ \mathrm{cm}^{-2}]$
$norm_{relxill}$	$7^{\dagger}$	$[10^{-6}]$
$Index1_{relxill}$	3^{*}	
$a_{relxill}$	0.99^{*}	
$Incl_{relxill}$	80^{*}	$[deg]$
$Rin_{relxill}$	-1^{*}	
$Rout_{relxill}$	135.58^{*}	
$\Gamma_{relxill}$	$2.0^{+0.0}_{-0.8}$	
$Ecut_{relxill}$	300^{*}	
$logxi_{relxill}$	≤ 1.9	
$Afe_{relxill}$	$0.521^{+2.547}_{-0.022}$	
$refl\_frac_{relxill}$	$7.4^{+2.7}_{-7.0}$	
$norm_{bremss}$	0.0002^{*}	
kT_{bremss}	95^{+5}_{-31}	[keV]
$apec_{1,norm}$	$2.3^{\dagger}$	$[10^{-6}]$
kT_{apec_1}	$1.2^{+1.6}_{-0.9}$	[keV]
$apec_{1,abun}$	5^{+0}_{-5}	
$apec_{2,norm}$	8^{+4}_{-8}	$[10^{-5}]$
kT_{apec_2}	$0.7^{+13.2}_{-0.4}$	[keV]
$apec_{2,abun}$	$0.18^{+4.83}_{-0.13}$	
$E_{FeK\alpha}$	6.39^{*}	[keV]
$\sigma_{FeK\alpha}$	0.09 ± 0.05	[keV]
$norm_{FeK\alpha}$	$1.24^{+0.34}_{-0.27}$	$[10^{-5}]$
$E_{SiK\alpha}$	1.8^{*}	[keV]
$\sigma_{SiK\alpha}$	$0.06^{+0.13}_{-0.06}$	[keV]
$norm_{SiK\alpha}$	$1.6^{+2.2}_{-1.5}$	$[10^{-6}]$
$E_{5\,keV}$	$4.85^{+0.30}_{-0.68}$	[keV]
$\sigma_{5\,keV}$	1.3 ± 0.4	[keV]
$norm_{5\,keV}$	10^{+7}_{-6}	$[10^{-5}]$
$MOS2\ constant.factor$	1.020 ± 0.023	
χ^2/d.o.f.	528.12/515	

Table 6.6: Best fit parameters for the relxill model fit of the X-ray spectra from pn and MOS2 with an additional emission line at 5 keV and the calculated errors. Parameters indicated with a $*$ have been frozen during the fitting process. The † signifies a parameter whose error calculation did not converge.

7 Summary and Outlook

This thesis focused on an X-ray observation of NGC 1052 by *XMM-Newton* and studied the lightcurves of the EPIC cameras and the spectra in detail.
The standard qualifiers for generating a GTI file were not sufficient in this extraction, such that an external GTI file was used. The final extracted lightcurves showed no variability.
The X-ray spectra of NGC 1052 were fitted using standard spectral model components from (Fabian, 2006). Within this work, two models with different physical properties, one assuming a partially covered source and the other assuming relativistic broad line emission, were tested and compared. The soft X-ray component was described by a thermal plasma and a highly absorbed powerlaw, for which a partial covering absorber was used. The other model, called relxill, is based on relativistic Compton reflection. Within this model fit, no evidence for a relativistically broadened $Fe\ K\alpha$ emission could be found for this source as suggested in previous analyses, e.g. Boeck (2012). However, an emission line at 5 keV was found in the pn spectrum, which has not been detected in previous observations and would require a study to examine the origin of that line further.
Because the relxill model is very complex and considers many physical features, further analysis is needed to investigate the physical quantities of the spectrum. This can be realized either by observations with longer exposure times or by an observation with *NuSTAR*, which already observed NGC 1052 simultaneously to the *XMM-Newton* observation studied in this thesis. *NuSTAR* covers an energy range from 3-78 keV[1], which would yield an energy overlap from 3-10 keV for both *XMM-Newton* and *NuSTAR*. Using both observations together for a detailed analysis of the spectrum can lead to the answer of the question, whether the radio-loud AGN NGC 1052 shows an evidence for a broad $Fe\ K\alpha$ line.

[1] *NuSTAR*(https://heasarc.gsfc.nasa.gov/docs/nustar/nustar_tech_desc.html, March 28, 2019)

Bibliography

Abdikamalov A.B., Ayzenberg D., Bambi C., et al., 2019, arXiv e-prints

Arnaud K., Smith R., Siemiginowska A., 2011, Handbook of X-ray Astronomy

Baczko A.K., Schulz R., Kadler M., et al., 2016, Astronomy and Astrophysics 593, A47

Beckmann V., Shrader C.R., 2012, Active Galactic Nuclei

Bergmann L., Schaefer C., Raith W., 2002, Lehrbuch der Experimentalphysik - Sterne und Weltraum, Walter de Gruyter, 2 edition

Boeck M., 2012, Dissertation, Friedrich-Alexander-Universitaet Erlangen-Nuernberg

Brenneman L.W., Weaver K.A., Kadler M., et al., 2009, Astrophysical Journal 698, 528

Carter J.A., Read A.M., 2007, Astronomy and Astrophysics 464, 1155

Dauser T., 2010, Ph.D. thesis, Astronomisches Institut der Universitaet Erlangen-Nuernberg

Dauser T., García J., Walton D.J., et al., 2016a, Astronomy and Astrophysics 590, A76

Dauser T., García J., Wilms J., 2016b, Astronomische Nachrichten 337, 362

Dauser T., Garcia J., Wilms J., et al., 2013, Monthly Notices of the Royal Astronomical Society 430, 1694

ESA 2012, XMM-Newton Users Handbook Issue 2.10

Fabian A.C., 2006, Astronomische Nachrichten 327, 943

Fanaroff B.L., Riley J.M., 1974, Monthly Notices of the Royal Astronomical Society 167, 31P

García J., Dauser T., Reynolds C.S., et al., 2013, Astrophysical Journal 768, 146

Gehrels N., 1986, Astrophysical Journal 303, 336

Giacconi R., 2003, Reviews of Modern Physics 75, 995

Guainazzi M., 2000, In: AAS/High Energy Astrophysics Division #5, Vol. 32. Bulletin of the American Astronomical Society, p. 1204

Guainazzi M., Oosterbroek T., Antonelli L.A., Matt G., 2000, Astronomy and Astrophysics 364, L80

Houck J.C., Denicola L.A., 2000, In: Manset N., Veillet C., Crabtree D. (eds.) Astronomical Data Analysis Software and Systems IX, Vol. 216. Astronomical Society of the Pacific Conference Series, p. 591

Howell S.B., 2006, Handbook of CCD Astronomy

Hoyle F., Fowler W.A., 1963, Monthly Notices of the Royal Astronomical Society 125, 169

Kadler M., 2004, XMM-Newton Proposal 03062301, XMM-Newton Proposal

Kadler M., Kerp J., Ros E., et al., 2004, Astronomy and Astrophysics 420, 467

Kadler M., Ros E., Kerp J., et al., 2002, In: Ros E., Porcas R.W., Lobanov A.P., Zensus J.A. (eds.) Proceedings of the 6th EVN Symposium., p. 167

Kellermann K.I., Sramek R., Schmidt M., et al., 1989, AJ 98, 1195

Kellogg E., Baldwin J.R., Koch D., 1975, Astrophysical Journal 199, 299

Knapp G.R., Gallagher J.S., Faber S.M., 1978, Astronomical Journal 83, 139

Krolik J.H., 1999, Active galactic nuclei : from the central black hole to the galactic environment

Lumb D.H., Warwick R.S., Page M., De Luca A., 2002, Astronomy and Astrophysics 389, 93

Mushotzky R.F., Cowie L.L., Barger A.J., Arnaud K.A., 2000, Nature 404, 459

Santangelo A., Madonia R., 2014, Astroparticle Physics 53, 130

Schneider P., 2015, Extragalactic Astronomy and Cosmology: An Introduction

Seyfert C.K., 1943, Contributions from the Mount Wilson Observatory / Carnegie Institution of Washington 671, 1

Strüder L., Briel U., Dennerl K., et al., 2001, Astronomy and Astrophysics 365, L18

Turner M.J.L., Abbey A., Arnaud M., et al., 2001, Astronomy and Astrophysics 365, L27

Urry C.M., Padovani P., 1995, Publications of the Astronomical Society of the Pacific 107, 803

Weaver K.A., Wilson A.S., Henkel C., Braatz J.A., 1999, Astrophysical Journal 520, 130

Danksagung

Nun möchte ich noch allen Menschen danken, die mir geholfen haben diese Arbeit zu schreiben und Ihr Wissen mit mir geteilt haben.
Zuerst möchte ich Matthias Kadler danken. Er hat mir ermöglicht diese spannende Arbeit über "seine" Quelle NGC 1052 zu schreiben und unterstüzte mich auf diesem Weg stets mit seinen fachgerechten Rückmeldungen und Diskussionen, welche die Qualität meiner Arbeit steigerten. Da diese Arbeit in enger Zusammenarbeit mit dem Astronomie Lehrstuhl an der Karl-Remeis Sternwarte in Bamberg entstanden ist, möchte ich mich ganz herzlich bei Jörn Wilms bedanken. Er war immer ein Ansprechparnter für jegliche Fragen. Ganz besonders möchte ich meiner Betreuerin, Andrea Gokus, danken. Sie ist mir ein Vorbild durch ihre zielstrebige Art. Sie war immer zu erreichen, obwohl sie nicht immer vor Ort war und hat sehr zu einer verbesserten Qualität dieser Arbeit beigetragen. Ebenfalls aus Bamberg, hat mir Thomas Dauser bei der Analyse der Spektren geholfen und ich danke ihm sehr für seinen hilfreichen Input.
Ich möchte mich bei Annika Kreikenbohm bedanken, die mich beim einführenden Praktikum zur Vorbereitung meiner Bachelorarbeit betreut hat, immer für meine Fragen da war sowie einige Kapitel Korrektur gelesen hat. Ihren Platz im Büro von Katharina Leiter und Marcus Langejahn einzunehmen, war für mich eine große Ehre. Katha und Marcus haben mir die Zeit im Büro am Lehrstuhl der Astronomie sehr angenehm gestaltet, weil es eine sehr lockere und lustige Atmosphäre war und beide stets sehr hilfsbereit waren. Man kann von beiden sehr viel lernen. Marcus danke ich auch für seine Geduld und die Verbesserungsvorschläge für meine Arbeit. Zusätzlich danke ich dem gesamten Astronomie Lehrstuhl und der AG Kadler für eine angenehme Atmosphäre.
Ich danke meinen Eltern Michaela und Stefan, sowie meiner Schwester Victoria, die immer hinter mir stehen und mich unterstützen. Zu guter Letzt möchte ich noch meinem Freund Antony danken, der mich während dieser Arbeit seelisch unterstützt hat und sonst auch immer für mich da ist.

Acknowledgements

This research has made use of a collection of ISIS functions (ISISscripts) provided by ECAP / Remeis observatory and MIT (http://www.sternwarte.uni-erlangen.de/isis/).
This thesis is based on observations obtained with *XMM-Newton*, an ESA science mission with instruments and contributions directly funded by ESA Member States and the USA (NASA).
This research has made use of the NASA/IPAC Extragalactic Database (NED), which is operated by the Jet Propulsion Laboratory, California Institute of Technology, under contract with the National Aeronautics and Space Administration.

Declaration

I, Constanze Seibert, declare that this thesis titled, 'X-ray analysis of the AGN NGC 1052 with XMM-Newton' and the work presented in it are my own. I confirm that:

- This work was done wholly or mainly while in candidature for a research degree at this University.
- Where any part of this thesis has previously been submitted for a degree or any other qualification at this University or any other institution, this has been clearly stated.
- Where I have consulted the published work of others, this is always clearly attributed.
- Where I have quoted from the work of others, the source is always given. With the exception of such quotations, this thesis is entirely my own work.
- I have acknowledged all main sources of help.
- Where the thesis is based on work done by myself jointly with others, I have made clear exactly what was done by others and what I have contributed myself.

Signed: _____

Date: _____